Year-round assessment of sea ice pressure ridges by multi-frequency electromagnetic induction sounding

Polona Itkin[1], Evgenii Salganik[2,1], Dmitry V. Divine[1], Arttu Jutila[3,2], Christian Katlein[2], Mara Neudert[2], Ian Raphael[4], Robert Ricker[5], and Egor Shimanchuk[6]

[1]Norwegian Polar Institute, Tromsø, Norway
[2]Alfred Wegener Institute, Helmholtz Centre for Polar and Marine Research, Bremerhaven, Germany
[3]Finnish Meteorological Institute, Helsinki, Finland
[4]Dartmouth College, Thayer School of Engineering, Hanover, New Hampshire, USA
[5]NORCE Norwegian Research Centre, Tromsø, Norway
[6]Arctic and Antarctic Research Institute, Saint Petersburg, Russian Federation

Correspondence: Polona Itkin (polona.itkin@npolar.no)

Abstract. ~~The thickness~~ Thickness and consolidation state of pressure ridges are ~~variables relevant for sea ice mass balance, melt processes and~~ relevant for determining sea ice volume and for understanding ecosystem habitat. We show how both variables can be detected ~~by the~~ using multi-frequency electromagnetic induction (EMI) sounding~~, based on data collected during Multidisciplinary drifting Observatory for the Study of Arctic Climate (MOSAiC) in the central Arctic Ocean between November 2019 and July 2020. We validate~~ . Our preliminary empirical approach shows that the in-phase channels of low frequency (1.5–18 kHz) give good estimates of total thickness, while quadrature channels of high frequency (18–93 kHz) give good estimates of consolidated layer thickness. The footprint size and sensitivity of the method make the EMI sounding appropriate for the detection of ridges with up to 10 m total thickness. We interpret and evaluate the EMI results by collocating them to sea ice topography from the airborne laser scanner, underwater topography from multi-beam sonar, ~~and~~ sea ice thickness and structure from drill holes ~~. Selected channels of low frequency give good estimates of total thickness, while selected channels of high frequency give good estimates of consolidated layer thickness.~~ and thermistor chain data collected during Multidisciplinary drifting Observatory for the Study of Arctic Climate (MOSAiC) in the central Arctic Ocean between November 2019 and July 2020. The MOSAiC EMI dataset was collected over a large number of ridge systems formed between freeze-up and break-up ~~. Nine~~ with nine individual ridge transects~~can be used to track the seasonal development. The footprint size and sensitivity of the method make the EMI sounding appropriate for the detection of ridges with up to 10 m total thickness. Where available, the ridge structure data from other methods are consistent with our results. The superior temporal and spatial coverage of the MOSAiC EMI data permits further analysis that~~ . The temporal evolution over this seasonal dataset indicates a slow reduction of the total thickness towards the consolidated layer thickness. Interestingly, the consolidated layer thickness exceeds the level ice thickness by a factor of 1.6 to 2 and also shows, at least for individual ridges, a seasonal decrease. This may be a feature of the thin snow cover at MOSAiC. Multi-frequency EMI is a promising method for non-intrusive pressure ridge surveying with a large potential for ~~pressure ridge dataset extension~~understanding of spatio-temporal processes within pressure ridges.

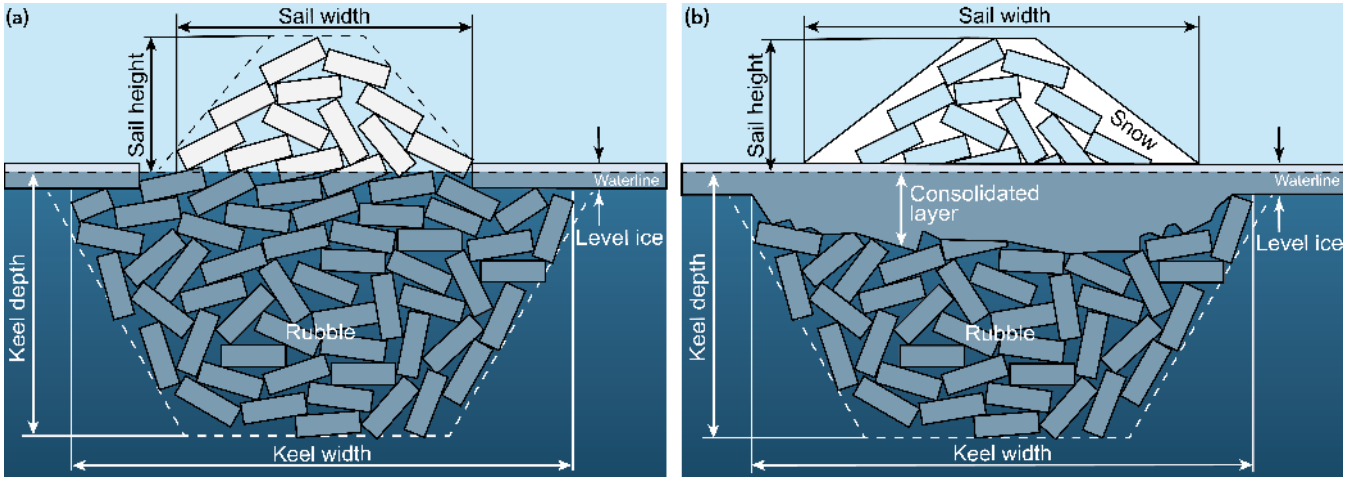


Figure 1. Schematics of a ridge cross-section showing dimensions of sail, keel, and adjacent level ice right after ridge formation (a) and after ridge consolidation (b).

1 Introduction

Approximately one-third of the Arctic sea ice area consists of pressure ridges (Melling and Riedel, 1996; Hansen et al., 2014; Brenner et al., 2021; Divine et al., 2025). Under ongoing climate change with increased drift speeds (Spreen et al., 2011), sea ice deformation is likely increasing (Rampal et al., 2009; Itkin et al., 2017; Rheinlænder et al., 2024). However, because the ice is generally thinner, the fraction of ice thicker than 5 m (Hansen et al., 2013; Sumata et al., 2023) and the overall occurrence of ridges ~~are~~ is decreasing (Krumpen et al., 2025). The roughness of deformed ice defines atmospheric and oceanic drag (Petty et al., 2017; Mchedlishvili et al., 2023) and influences snow accumulation and thermodynamic feedbacks (Itkin et al., 2023). Ridge thickness remains important for estimating ice volume and mean ice thickness (Pfaffling et al., 2007; Hendricks, 2009).

Ridges form complex 3-D structures in which ice blocks are separated by water-filled cavities (voids). The ratio of water-filled space to total underwater ridge volume defines the keel (macro-)porosity. Under cold atmospheric conditions, voids freeze and keel porosity decreases after ridge formation — a process called consolidation (Figure 1). The voids can also provide protected habitats for algae, zooplankton, fish, and mammals (Gradinger et al., 2010; Castellani et al., 2025).

The consolidation state is ~~important for navigation because~~ also important for mechanical strength of sea ice (Shafrova and Høyland, 2008). In navigation, consolidated ridges create major obstacles ~~, and they cause~~ causing the largest ice loads ~~when icebergs are absent (Ervik et al., 2019). It also affects the mechanical strength of sea ice (Shafrova and Høyland, 2008).~~ secondary only to icebergs (Ervik et al., 2019). In contrast, unconsolidated ridges act as weak lines in the icescape — damage lines that may reactivate (Oikkonen et al., 2017; Itkin, 2025). Numerical models now represent this principle as damage and healing (Ólason et al., 2026), but its characteristics remain open questions in sea-ice deformation studies.

Ridges form during convergent dynamic events, typically from thin ice with 0.2–0.4 m thickness based on measurements of ridge-block thickness (Strub-Klein and Sudom, 2012). Their underwater part is the keel, and the surface part is the sail. The

combined height of keel and sail is the total ridge thickness. The sail contains air- or snow-filled voids, while the voids in the keel are water-filled (Figure 1a). After formation, the water-filled voids (rubble) start freezing from the waterline downward, creating a void-free layer called the consolidated layer (CL) (Figure 1b). Although researchers often assume that the initial CL thickness is zero or equal to block thickness, direct observations remain rare (Figure 2b).

The main ridge morphological parameters — including sail and keel width and height — are typically correlated. For Arctic ridges, the maximum keel depth is 4.3±2.1 times the maximum sail height, and keels are ~~6.8~~3.8±~~4.6~~ 1.9 times wider than sails (Strub-Klein and Sudom, 2012). Ridge keels generally have a trapezoidal or triangular cross section (Ekeberg et al., 2015). These shape parameters are important in idealized ridge models (Tsamados et al., 2014) and when estimating ridge properties from observations of only one surface, such as draft from ULS or freeboard from satellite or airborne altimetry (Lange et al., 2025).

Ridge consolidation ~~is first analytically described~~ was first described analytically by Leppäranta and Hakala (1992), who relate the ratio of level-ice (LI) thickness to ~~consolidated layer (CL)~~ CL thickness to the square root of rubble porosity (η): $LI/CL = \eta^{0.5}$. This approach is valid when snow depth is similar on both ice types. Salganik et al. (2021) further developed the method to account for differences in snowpack, block thickness, and evolving environmental conditions. For a typical rubble porosity of around 30% (Figure 2a), the analytical solution of Leppäranta and Hakala (1992) estimates the CL to be about 1.8 times thicker than level ice. This estimate serves as an upper limit for winter field observations because surveyed ridges may be recently formed or accumulate thicker insulating snow than the surrounding level ice (e.g., Itkin et al., 2023). ~~Most winter observations~~ Winter observations generally show CL thicknesses 1.2~~–1.6 times larger~~ –1.6 times greater than surrounding level ice ~~, with lower values down to 0.6–0.7 observed by Kharitonov (2005) and Ervik et al. (2019) in spring~~ (Figure 2b).

In ~~contrast,~~ spring and summer~~observations often reveal a CL that is 2–4 times thicker than the surrounding level ice~~ , CL thickness can reach 2–4 times the surrounding level-ice thickness, although substantial variability remains (Figure 2b). Most second- and multiyear ridges that survive summer melt also remain fully consolidated, with nearly zero keel porosity ~~Shestov et al. (2012)~~(Shestov et al., 2012; Guzenko et al., 2025). To explain this, Marchenko (2022) formulated a thermodynamic model of ridge summer consolidation in which keel melt produces meltwater that later refreezes and increases consolidation. Lange et al. (2023), however, showed that snow meltwater can be the dominant source of summer consolidation. In addition, Salganik et al. (2023d) observed rapid ridge consolidation immediately after a lead-opening event, suggesting that snow–slush transfer into the ridge may rapidly reduce keel porosity and accelerate consolidation. Similarly, ~~Guzenko et al. (2024)~~ Guzenko et al. (2025) observed the strongest ridge consolidation in March, with only minor consolidation during summer.

~~As the thickest sea-ice features, first-year ridges typically melt 3–5 times faster than the surrounding level ice. This estimate comes from observations using moored sonars (Amundrud et al., 2006), thermistor strings (Shestov et al., 2018), and repeated surveys with ROV-mounted sonar (Salganik et al., 2023e), with deeper ridges melting even faster. In contrast, Perovich et al. (2003) observed only a 1.6-times faster melt for older multiyear ridges, which are usually fully consolidated, smoother, and therefore melt more slowly.~~

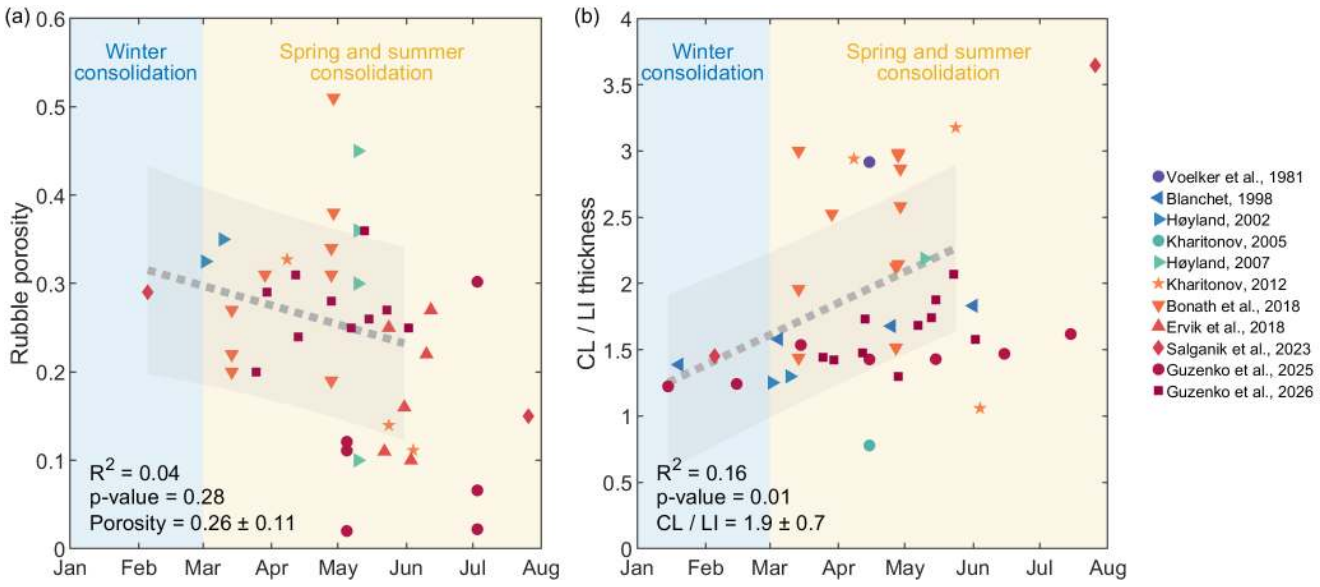


Figure 2. Seasonal evolution of rubble ~~macro-porosity~~ porosity η (a) and the ratio of consolidated layer (CL) ~~and~~ to level ice (LI) thicknesses (b) from historical drilling observations. ~~Results of linear regression are based on the measurements outside of the summer season, with the value of~~ Linear regressions and mean ± standard deviation ~~of all porosity~~ are calculated from observations before 1 June. The approximate seasonal transitions between winter consolidation, spring consolidation, and summer melt ~~are approximate and~~ depend on the ~~location~~ locations and conditions of individual measurements.

Ridges also alter the bulk density of sea ice, which plays an important role in hydrostatic balance and in converting satellite-derived freeboard to thickness (Landy et al., 2020; Petty et al., 2026). The density of sea-ice ridges is typically lower than that of first-year level ice (920 kg m^{-3}) and comparable to second-year level ice (880–910 kg m^{-3}), based on both air-
80 borne multi-sensor surveys (Jutila et al., 2022) and in-situ observations ~~(Richter-Menge and Cox, 1985; Salganik et al., 2025)~~ (Richter-Menge and Cox, 1985; Salganik et al., 2025; Guzenko et al., 2026). Snow density on ridges and level ice is similar ~~(Macfarlane et al., 2023; Itkin and Liston, 2024)~~(Macfarlane et al., 2023; Itkin and Liston, 2025), but ridges accumulate more than twice as much snow as level ice (Itkin et al., 2023).

All our knowledge on the internal structure of the ridges presented above originates from scarce and labor intensive ridge
85 drillings and similar intrusive methods. Electromagnetic induction (EMI) sounding for ground-based sea-ice thickness measurements has been in use since the 1990s (e.g. Eicken et al., 2001; Renner et al., 2014; Rösel et al., 2018; Itkin et al., 2023) and is also implemented in airborne sensors (e.g. Pfaffling et al., 2007; Hendricks, 2009; von Albedyll et al., 2022). This method is well established for detection of level ice thickness and it revolutionized the traditional direct measurements by drilling. While commonly used EMI sensors operate at a single frequency, or use only one frequency to detect sea-ice thick-
90 ness, ~~Hunkeler et al. (2016)~~ Hunkeler et al. (2015) and Neudert et al. (2024) use information from several channels of multi-frequency EMI devices operating between 1 and 90 kHz to detect porous layers of platelet ice beneath consolidated landfast

ice in Antarctica. Such detection of porosity by EMI may be relevant also for the survey of the internal structure of ridges, but it was not explored to this date. The porosity of the platelet layer results from the accumulation of loose disc-shaped platelet crystals in seawater below consolidated ice. ~~Porosity of sub-ice platelet ice is typically around 80%, but ranges from below 50% to as high as 94% (Hoppmann et al., 2020).~~ The crystals are usually up to 10 cm in diameter, and their accumulation creates small water-filled pockets an order of magnitude smaller than ridge voids, forming an ice matrix with micro-porosity ~~.~~

~~Results from Hunkeler et al. (2016) and Neudert et al. (2024) indicate that the conductivity of this saline porous layer is sufficient to detect the interface between consolidated and unconsolidated ice when using frequencies of 1–90 kHz~~values typically around 80%, but ranging from below 50% to as high as 94% (Hoppmann et al., 2020). Because the EMI instrument footprint is approximately four times larger than the level-ice thickness (Reid and Vrbancich, 2004), we hypothesize that the ~~macro-porosity of unconsolidated ridge layers~~ average rubble porosity within such ice volume can be detected by EMI in a manner similar to the micro-porosity of loose platelet-ice layers.

During the ~~MOSAiC drift~~ Multidisciplinary drifting Observatory for the Study of Arctic Climate (MOSAiC) expedition (Shupe et al., 2020; Nicolaus et al., 2022) from October 2019 to July 2020, researchers observed seasonal pressure ridge evolution over an extensive area with a radius of approximately 2 km around the centrally placed research vessel (RV) *Polarstern*. This area, consisting of mixed ice types, is called the MOSAiC Central Observatory (CO). The ice types in the CO included 1) deformed second-year ice (SYI), 2) level SYI, and 3) first-year ice (FYI) ~~(Webster et al., 2022; Itkin et al., 2023; Guo et al., 2023; Itkin and~~ (Webster et al., 2022; Itkin et al., 2023; Guo et al., 2023; Itkin and Liston, 2025). Over the winter, several deformation events formed and modified ridge systems, some of which researchers surveyed using drillings, temperature sensors, and underwater sensors (Salganik et al., 2023e), or sampled for chemical and ecological parameters ~~(Lange et al., 2023)~~(Lange et al., 2023; Müller et al., 20

.

Researchers outlined the general characteristics of the seasonal increase in deformed ice using airborne EMI datasets (von Albedyll et al., 2022) and satellite Synthetic Aperture Radar (SAR) datasets (Guo et al., 2023; Kortum et al., 2024). Ridge statistics over a larger area were extracted from airborne laser scanner (ALS) data collected in March 2020 (Ricker et al., 2023). Some ridges were also profiled with ground-based multi-frequency EMI transects, which Webster et al. (2022) and Itkin et al. (2023) analyzed with a focus on ice–snow interactions. For example, ~~Itkin et al. (2023) shows~~ Itkin et al. (2023) showed that most of the snow volume sampled in transects accumulates in the ridges. However, researchers have not yet analyzed ice porosity and consolidation within the ridge EMI transects.

This paper aims to 1) provide a comprehensive description of the ridges at the MOSAiC CO, 2) evaluate ground-based multi-frequency EMI ridge transects using ridge porosity and consolidation data from ice drillings, snow freeboard from ALS, and ~~draft from ROV-mounted sonar~~ ice draft from sonar mounted on a remotely operated vehicle (ROV), and 3) estimate the spatial extent of ridge porosity and the temporal development of winter ridge consolidation at the MOSAiC CO using ground-based multi-frequency EMI transects.

2 Methods and data

2.1 EMI transects

We use a multi-frequency EMI sensor (GEM-2, Geophex Ltd, USA). The instrument includes a real-time data processing unit with a ~~GPS~~ GNSS receiver, which communicates with a field PC that operates the sensor and records EMI and GPS data streams. The GEM-2 transmits and records multiple configurable frequencies in the kHz range simultaneously at a sampling rate of ~~10~~ 20 Hz. In this study, we use five frequencies with approximately logarithmic spacing across the sensor's frequency range: 1.5, 5.3, 18, 63, and 93 kHz.

The instrument generates a primary EM field H_p, which induces a secondary EM field H_s in the seawater within its footprint. In ground-based surveys, the distance from the instrument, placed directly on top of the sea ice, to the seawater determines the ice thickness. The basic principle of EMI sounding is to convert the measured ratio of secondary to primary field strength, H_s/H_p, into the distance to seawater, z_{iw}. H_s/H_p can refer to the in-phase or quadrature components, i.e., the real and imaginary parts of this complex ratio. The conversion uses an empirical exponential approximation (Haas et al., 1997; Pfaffling et al., 2007):

$$H_s/H_p = c_0 + c_1 \exp(-c_2 z_{iw}). \tag{1}$$

Here, c_0, c_1, and c_2 are calibration parameters determined from measurements over sea ice of known thickness. To obtain them, we place the GEM-2 at seven known, equally spaced heights from 0 to 2 m above a level sea-ice surface using a wooden ladder and record the EMI response for at least 10 s at each height. Afterwards, we measure sea-ice thickness by drilling five holes through the ice and add the average thickness to the calibration heights. This procedure provides seven calibration distances (z_{iw}) in the range of approximately 0.5 to 5 m, depending on the level-ice thickness.

The calibration procedure follows Itkin et al. (2023), except that they use only the 18 kHz in-phase channel, while we reprocess the original data published by Hendricks et al. (2022) and apply the calibration to all channels. We perform calibration at least weekly, and we use the closest-in-time calibration curves for each survey to retrieve distances. In some cases, data from certain channels malfunction, limiting the amount of available data. We also exclude any data that fail the quality control of Itkin et al. (2023). We take care to avoid EMI responses from any other electrically conductive material within the instrument footprint. Following Reid and Vrbancich (2004), we approximate the GEM-2 footprint as four times the total ice thickness. Instrument noise measured on landfast ice in Antarctica reaches up to 5% of the signal (Neudert et al., 2024). Since the noise follows a Gaussian distribution, we assume it can be effectively mitigated by averaging over a short period (e.g., 10 s, which averages ~~100~~ 200 measurements). To avoid measurement drift, we always leave the GEM-2 outside to reach ambient temperatures before each survey (Itkin et al., 2023).

CL is the distance between the waterline and the beginning of the porous rubble inside the ridge. The conductivity of solid sea ice above and below the water line is sufficiently similar, that boundary is not detectable by EMI. Only the boundary between the consolidated layer and rubble has a sufficient porosity and conductivity difference. Thus, EMI retrieves the distance from

the snow surface to the bottom of the CL, given by $z^*_{cl} = z_{cl} + z_f + z_s$, where z_f is ice freeboard and z_s is snow depth. If z_f and z_s are known, CL can be calculated from CL*.

We assume that level sea ice is fully consolidated and has very low electrical conductivity; therefore, the total and ~~CL~~ CL* thicknesses coincide and yield similar solutions for all 10 channels (in-phase and quadrature components of each of the five frequencies). Due to the different sensitivity of individual EMI channels—especially quadrature—to sea-ice conductivity (Hunkeler et al., 2016; Neudert et al., 2024), we expect solutions to diverge over porous sea ice, such as unconsolidated ridges. ~~Neudert et al. (2024)~~ Neudert et al. (2024) also analyzed the sensitivity of individual channels to noise, instrument roll, and conductivity. Reid et al. (2003) examined the influence of instrument pitch on retrieval with a single-frequency instrument. Their findings show that instrument roll and pitch introduce significant overestimation, particularly in in-phase channels. They also find that high-biased sea-ice conductivity, as expected for ice–seawater mixtures in porous keels, causes a disproportionately large underestimation of sea-ice thickness in quadrature channels compared to in-phase channels.

We surveyed sea ice using small-scale EMI transects at several ridge observatories (Section 2.9.1). For these transects, we operated the instruments at discrete points spaced 1 m apart along a survey tape measure, holding the instrument as horizontally as possible to minimize pitch and roll. For March–May transects over the same ridge cross-sections, we towed the instrument on a sled (without control over pitch and roll) and calculated EMI averages for all channels at snow-depth measurement locations spaced roughly 1 m apart.

In addition to these point transects, which cover less than 1 km in total, we conducted approximately 60 km of 'standard' sled transects over predominantly level ice in the CO, spread seasonally from November 2019 to July 2020 with roughly weekly frequency (Itkin et al., 2023). We towed the GEM-2 on a sled, while simultaneously recording snow depth at points spaced 1–3 m apart. We also operated the GEM-2 sled along tracks to various sites during reconnaissance trips, although we did not collect snow-depth measurements for these transects.

Subsections of these standard transects crossed ridges. Because we performed them without a survey tape measure, simply by retracking a route along flags spaced about 50 m apart, their positions are less precise and harder to co-locate than the point transect measurements at the ridge observatories. We collected the EMI signal at walking or driving speed (when using a snowmobile). The instrument in the sled tilts while crossing ridge sails, which introduces significant overestimates of total ridge thickness (Neudert et al., 2024). However, such transects take roughly ten times less time and provide an important data source to upscale the point ridge transects to the broader area.

2.2 Snow depth

Along all EMI transects, except those towed by the snowmobile, snow depth measurements were collected using an automated snow depth probe, Magnaprobe, by SnowHydro LLC (Sturm and Holmgren, 2018). ~~The spacing interval of the snow-depth measurements was~~ Snow depth measurements used in this study were spaced by approximately 1 ~~to 3 m~~ m (Itkin et al., 2021).

2.3 Drill holes

We made drill holes using a 2-inch diameter ice auger (Kovacs Enterprise, USA). Each ridge transect contained 8–11 drilling locations where we measured snow depth, freeboard, and total ridge ice thickness. We also estimated the thickness of the CL based on the water content in the drilling residuals and voids, as well as the softness of the drilled ice. ~~The drill hole data~~ Keel porosity was estimated from the cumulative thickness of water-filled voids relative to the total sampled keel depth, whereas rubble porosity was calculated over the unconsolidated portion of the keel. The drill-hole data used in this study are published in Salganik et al. (2023a, 2022). Drill-hole porosity estimates are subject to uncertainty in identifying water-filled voids and the consolidated-layer boundary from drilling resistance and residuals. Their representativeness is further limited by the strong spatial heterogeneity of ridge structure and the small sampling volume of individual boreholes. Drill-hole measurements are used in this study as independent point-scale observations to validate EMI-derived keel and CL thickness.

2.4 Thermistor chains

We study the temporal evolution of ridge interfaces ~~and temperatures using~~ using temperature measurements from ice mass balance buoys (IMB). We deployed two types of IMBs: the Snow Ice Mass Balance Apparatus (SIMBA, SAMS Enterprise Ltd, UK) and the Digital Thermistor Chain (DTC, Bruncin d.o.o., Croatia). SIMBAs have sensors spaced 2 cm apart and provide temperature readings every 6 h with an accuracy of 0.1°C. Daily internal heating cycles of 30 s and 120 s allow us to identify the locations of air–snow, snow–ice, and ice–water interfaces with high precision (Jackson et al., 2013). DTC sensors also have 2 cm spacing and record in situ temperature and post-heating temperature after a 20 s cycle every 6 h with an accuracy of 0.25°C (Salganik et al., 2023). We manually identify the location of each interface using a combination of in situ and post-heating temperature data. In general, the response of air and water to heating cycles shows large temporal variability, whereas the snow–ice interface exhibits a pronounced change in the vertical temperature gradient. The location of the bottom interface of the CL was identified assuming a nearly zero vertical temperature gradient below it following Salganik et al. (2021); given the known vertical reference of the borehole and approximately constant water level, this directly yields the CL thickness.

2.5 Airborne Laser Scanner (ALS) snow freeboard

The helicopter-based ALS Riegl VQ-580 (Horn, Austria) provides sea-ice surface elevation values with kilometer-scale areal coverage, 0.5 m spatial resolution, and 0.025 m accuracy. We convert ALS elevation measurements to snow freeboard using an automated open-water detection scheme based on differences in laser reflectance (Hutter et al., 2023a, b). Snow freeboard is the distance between the water line and the top of the snow (or ice surface in the case of bare ice).

In this study, we use only one ALS grid from 21 January ~~2020.~~ 2020, with a modal freeboard uncertainty of 0.26 m. This scan covers the entire CO area well and was acquired before major snowfall and snow redistribution events.

2.6 Multibeam (MB) sonar draft

The MB sonar (DT101, Imagenex, Canada) mounted on a remotely operated vehicle (ROV; M500, Ocean Modules, Sweden; after Katlein et al. (2017) and Anhaus et al. (2025)) measures ice draft over an area approximately 350 m in diameter, with 0.05 m vertical accuracy and 0.5 m horizontal resolution (Coppolaro, 2018). Distance from ROV to ice was converted to ice draft using pressure sensor measurements.

In this study, we use only two MB scans from 7 and 28 January ~~2020.~~ 2020 (Katlein et al., 2022). The first scan covers a wide area and we use it for plotting, while the second is a high-resolution scan of the Fort Ridge observatory taken close in time to the ALS flight.

2.7 Co-location and bias correction of the data

Each data source described above has a GPS position at the time of sampling. However, because the sea ice constantly drifts, achieving exact relative positioning between datasets is challenging. We first convert all positions to a local coordinate system (Itkin et al., 2023) relative to the RV *Polarstern* positions and heading on 15 October 2019, and back-track all sampling positions to that reference date. We then apply a sequence of manual lateral shifts and rotations~~to achieve an approximate positioning accuracy of 10 m~~. The steps are:

1. We consider the backtracked local coordinates of the ALS as the reference positions and adjust all other positions to best fit them.
2. We use ridge drilling and EMI transect metadata, including fieldwork photographs and notes on sail crest and instrument locations, to adjust their positions atop the ALS snow freeboard.
3. We estimate the waterline from drill-hole freeboard measurements and bias-correct the ALS snow freeboard accordingly.
4. We use drill-hole draft measurements to bias-correct the MB sonar draft.

Based on the source dataset absolute positioning accuracy and our observer expertise with the collection of the datasets, we estimate that the approximate relative positioning accuracy of the co-located data may be within 1 m.

2.8 Thermodynamic modeling

~~To predict the temporal evolution of the CL under environmental forcing, we use a~~ We simulate CL growth using the one-dimensional thermodynamic model ~~from Salganik et al. (2021)for the EMI and snow depth transects~~of Salganik et al. (2021), which describes heat conduction through snow and consolidated ice and freezing of water-filled voids in the underlying rubble. We initialize the model ~~at the time of the first measurement for each transect~~with the total and CL thickness at the first EMI survey and run it independently at each location along the ridge transects. We linearly interpolate snow ~~thickness between the times of each transect for every location. We assume~~ depth between surveys and assume a snow thermal conductivity of 0.26 W m^{-1} K^{-1} ~~for snow on ridges~~ (Macfarlane et al., 2023). We ~~estimate the initial ice freeboard as the difference~~

~~between the ALS snow freeboard and the snow thickness from the transects, and we estimate the initial CL thickness using EMI. We measure~~ use air temperature and wind speed ~~with~~ from the Atmospheric Surface Flux Station ASFS30 (Cox et al., 2023a, b) ~~. We determine ridge porosity from drilling measurements and assume it remains constant for each location of the two ridges. We estimate ridge thermodynamic parameters (~~and ocean temperature from the MOSAiC microstructure profiler measurements (Schulz et al., 2022) as model boundary conditions. Ocean heat flux at the CL boundary should be small and is neglected (Høyland, 2002). We assume a constant unconsolidated rubble porosity of 0.29 for all modeled locations, consistent with drill-hole observations (Salganik et al., 2023a, 2022). We derive ice thermal conductivity, density, and effective latent heat ~~) from salinity measurements of cores (Salganik et al., 2023b) and temperature data from thermistor chains~~from ice core salinity (Salganik et al., 2023b) and thermistor chain temperature measurements.

2.9 Ridges at the MOSAiC CO

This section describes the pressure ridge evolution in the MOSAiC CO based on on-site observations (Rex and Nicolaus, 2023; Haas and Rabe, 2023; Kanzow and Damm, 2023), ship radar animations (Krumpen et al., 2021a, c, b), Planet Labs PBC satellite images (Salganik et al., 2023d), a RADARSAT-2 image (Itkin et al., 2023), and TerraSAR-X images (Guo et al., 2023). We group all large ridge systems month by month according to their formation date, resulting in 35 ridge systems divided into 5 groups. Figure 3 shows these ridge systems overlaid with ALS-derived snow freeboard from 21 January 2020. We backtrack any lateral displacements or rotations using a local coordinate system (Nicolaus et al., 2022; Itkin et al., 2023). The accuracy of positions decreases with distance from the CO center at the RV *Polarstern* and the transect tracks. After the beginning of March, we do not map all new ridge systems because deformation becomes frequent, and the CO starts to break up first along its starboard side and shortly after in the area ahead of the ship. By June, only about one-fourth of the original CO remains (lower right corner of Figure 3). The month-by-month groups of ridge systems are listed below.

- **Old ridges**: The port (right-hand) side of the CO consists of SYI or older ice and shows heavy deformation with deep refrozen melt ponds (Itkin et al., 2023). A data-model fusion study by ~~Itkin and Liston (2024)~~ Itkin and Liston (2025) suggests that snow begins accumulating here in August, while level ice thickness does not increase until the first MOSAiC observations in October and November. This part of the CO is called the 'Fortress' and likely contains ~~multi-year~~ multiyear ridges converted to hummocks by summer melt. Additional large ridges form in the Fortress during freeze-up. By the time the CO is established in October, both types of ridges are indistinguishable and marked gray in Figure 3.

- **October ridges**: The starboard (left-hand) side of the CO is nearly level and heavily ponded SYI with shallow, bottomless ponds typical of melting FYI (Itkin et al., 2023). After freeze-up in September (Itkin and Liston, 2025), the melt ponds refreeze, and surrounding open water further off the ship turns into FYI. RV *Polarstern* arrives at the CO at the beginning of October, so ridge formation occurs in all three ice types (deformed SYI, level SYI, and FYI). October ridges are shaded blue in Figure 3.

- **November–December ridges**: Strong deformation in mid-November drives the formation of many ridges, with additional ridges forming throughout December. These ridges are shaded yellow in Figure 3.

Table 1. Overview of the EMI ridge transects at MOSAiC

Transect Name	Ridge Name	Formation Date	Ice Type	Drilling Date	EMI transect date
Optics Transect	Fort Ridge	mid-October	SYI/FYI	24 Jan, 31 Jan	31 Jan
Installation transect	Fort Ridge	mid-October	SYI/FYI	8 Jan	8 Jan, 21 Feb
Coring transect	Fort Ridge	mid-October	SYI/FYI	17 Jan, 12 Feb	10 Jan, 12 Feb, 5 Mar
Southern transect	Allie's Ridge	4-5 January	SYI/lead	-	12 Feb, 28 Feb, 10 Apr
Central transect	Allie's Ridge	4-5 January	SYI/lead	17 Jan, 5 Feb	17 Jan, 31 Jan, 28 Feb, 10 Apr, 28 Jun
Northern transect	Allie's Ridge	4-5 January	SYI/lead	-	12 Feb, 28 Feb, 10 Apr
Nloop	Fortress	Old ridges and October	SYI	-	28 Nov – 7 May
Sloop	Sloop	October, November	SYI	-	5 Dec – 7 May
MeltMix	Fortress and FYI	Mix	Mix	-	29 Jun – 20 Jul

- **January–February ridges**: Formed during a relatively quiescent period with few deformation events in the CO. These ridges are shaded pink in Figure 3.

- **March–April–May ridges**: Formed during a sequence of strong deformation events that gradually break up the original CO, restricting survey work to a small area around the Fortress. After this point, it is no longer clear which deformation events produce ridges and which remain as leads.

Since late May, the MOSAiC CO does not show any new consolidating ridges. We assume that any deformation after this date causes breakup, as the sea ice drift transitions from winter linear-kinematic motion to summer granular flow of small individual floes (Nicolaus et al., 2022).

Table 1 shows an overview of all ridge transect measurements at MOSAiC.

2.9.1 Fort Ridge and Allie's Ridge observatories

In January, we established dedicated ridge observatories near RV *Polarstern* (Figure 4) on a ridge section formed in October (Fort Ridge) and on another formed in January (Allie's Ridge). At these observatories, we collected a suite of data from EMI transects, ridge drilling, thermistor chains, ALS, and MB sonar scans.

Fort Ridge formed in mid-October between a wide lead that opened between pieces of the Fortress ~~Rex and Nicolaus (2023); Itkin et al. (2~~ (Rex and Nicolaus, 2023; Itkin et al., 2023). Its block thickness ranged from 0.1 m on the FYI (lead) side to 0.8 m on the SYI side. This ridge provides an example of a double-sail structure built from SYI with several fracture zones and FYI on both flanks. The thinner, denser FYI (lead) blocks were pushed under the SYI. During winter, ridge drilling yielded an average snow depth of 0.4 m, a sail height of 0.4 m, a keel ~~draft~~ depth of 4.3 m, and a ~~total macro-porosity~~ keel porosity of 0.26–0.33 (Salganik et al., 2023a). After a sequence of deformation events in mid-March, Fort Ridge became inaccessible for direct measurements. This observatory included three nearly parallel cross-section transects:

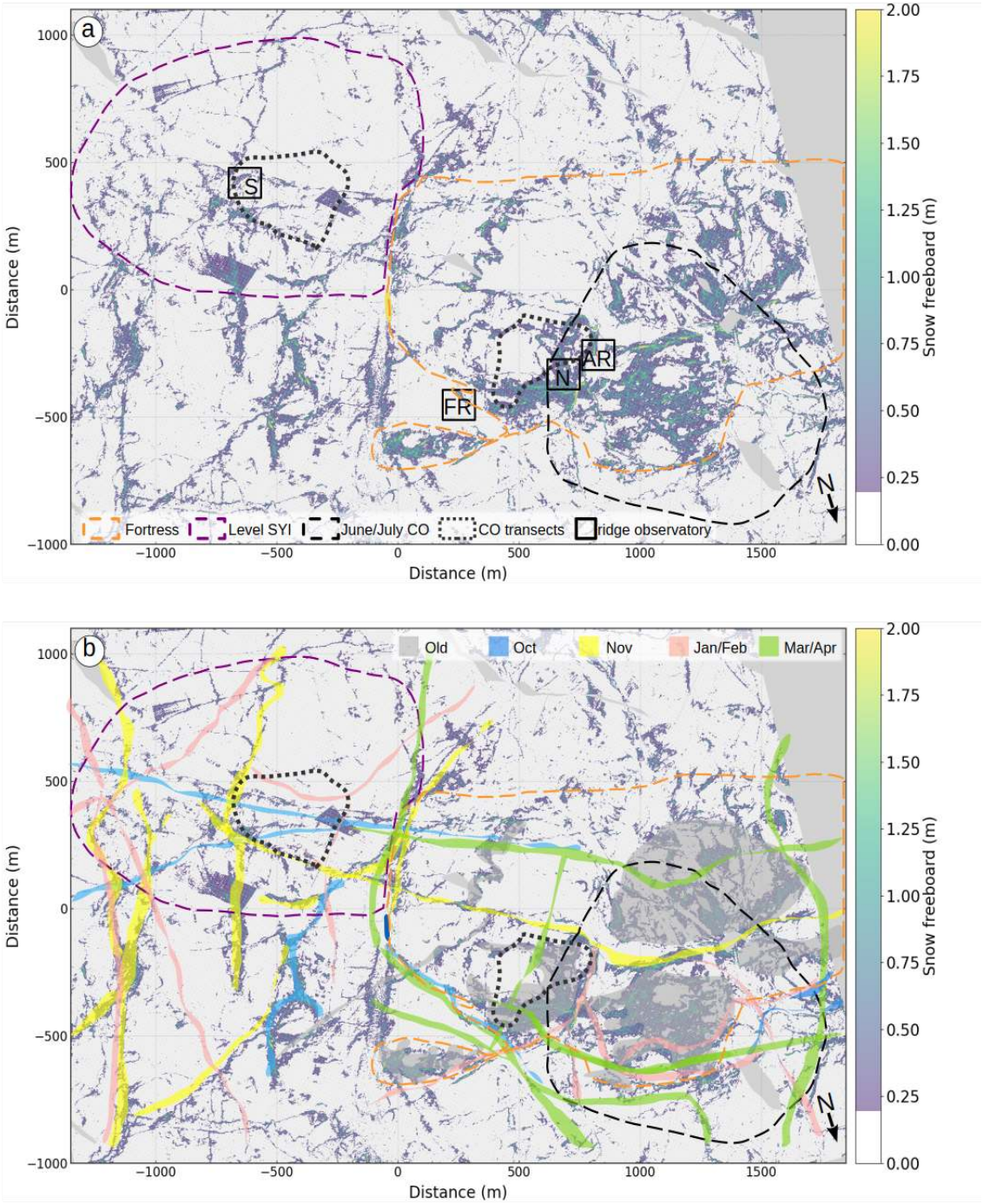


Figure 3. Ridges at the MOSAiC Central Observatory on the ALS snow ~~snow~~ freeboard from 21 January 2020. The areas with the lowest 10% of the values are white ~~patches~~ (level ice) and the areas not covered by the survey are ~~missing~~ gray (no data). RV *Polarstern* is in the center of the map, and the map is oriented in a way that the ship's heading in October points to the top of the figure. The ice types outlined on the map coincide with those published in ~~Itkin and Liston (2024)~~ Itkin and Liston (2025) and Guo et al. (2023). In June and July, only a subsection of the CO area was preserved. Panel a) shows locations of the ridge observatories (FR=Fort Ridge, AR=Allie's Ridge), standard transects (from left to right: Sloop, Nloop, MeltMix) with selected ridge crossings (N=Nloop, S=Sloop) and b) shows known formation dates of the major ridges shaded by colors.

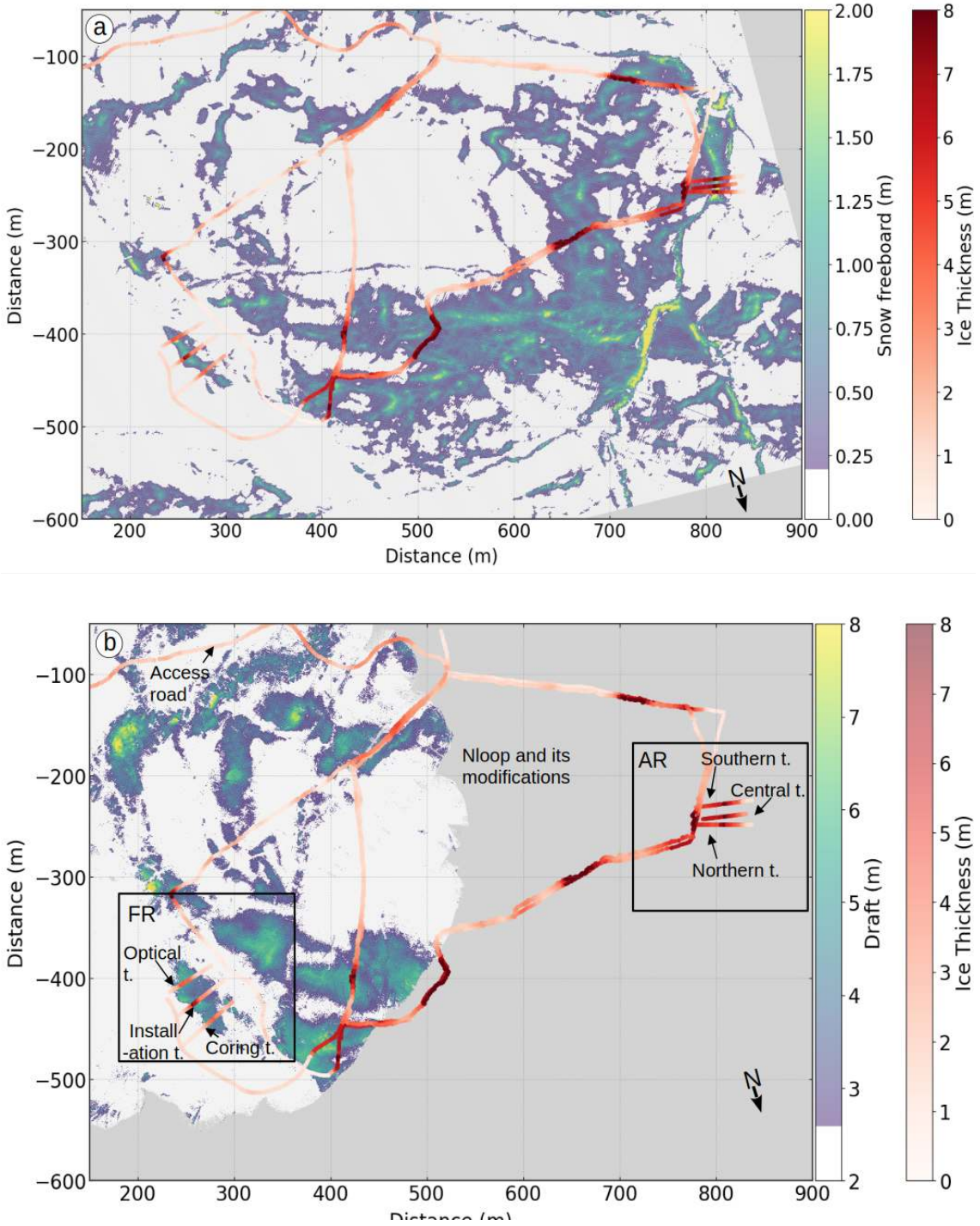


Figure 4. Ridges in the extended area of the winter ridge observatories on the ALS snow freeboard from 21 January 2020 and MB ice bottom topography (draft) from 7 January 2020. The areas with the lowest 10% of the values are white (level ice) and the areas not covered by the survey are gray (no data). The EMI transects ~~of~~ along Nloop, Fort Ridge (FR) and Allie's Ridge (AR) ~~transects~~ are annotated. A close-up of FR and AR is given in Appendix A in Figures A1 and A2.

- ~~**Optics transect**, with one EMI transecton 31 January; we drilled on 24 and 31 January.~~
- ~~**Installation transect**, with two EMI transects on 8 January and 21 February; we also drilled on 8 January, and this site became a major deployment location with three thermistor chains and other instruments.~~
- ~~**Coring transect**, with three EMI transects on 10 January, 12 February, and 5 March; drilling and biological coring were conducted on 17 January and 12 February.~~

Optics transect, Installation transect and Coring transect.

Allie's Ridge formed on 4–5 January at the edge of the lead that opened during ice-dynamics events on 7–15 December 2019. The ridge extended about 400 m and connected to a system of ridges in the CO. Its southern flank consisted mainly of thin lead-ice blocks 0.2–0.4 m thick, while the northern flank contained thicker second-year ice 0.9–1.0 m thick. Ridge drilling in January and February yielded an average snow depth of 0.14 m, a sail height of 0.7 m, a keel ~~draft~~ depth of 5.8 m, a keel ~~macro-porosity~~ porosity of 0.22, and a rubble ~~macro-porosity~~ porosity of 0.29 (Salganik et al., 2022). We collected data along three cross-profiles:

- ~~**Southern transect** with three EMI profiles on 12 February, 18 February, and 10 April.~~
- ~~**Central transect** with five EMI profiles on 17 January, 31 January, 28 February, 10 April, and 28 June. We drilled on 17 January and 5 February, and we installed two thermistor chains.~~
- ~~**Northern transect** with three EMI profiles on 12 February, 18 February, and 10 April.~~

Southern transect, Central transect and Northern transect.

We installed five thermistor chains at the ridge observatories. On Fort Ridge, the SIMBA 2020T60 (T60) temperature buoy was installed near the ridge center (operational until 22 April), and DTC24 and DTC25 were installed on the ridge flanks (operational until mid-March). T60 had a much smaller initial snow depth (0.1 m) than DTC24 (0.8 m) and DTC25 (0.5 m). On Allie's Ridge, the SIMBA 2020T61 (T61) buoy was installed near the keel center, and DTC26 was installed near the ridge flank, both on the lead side of the ridge.

2.9.2 Standard transects

At MOSAiC, we performed standard transects along flagged routes at approximately weekly intervals (Figure 3). These transects covered mainly level ice with occasional ridge crossings. The full MOSAiC transect dataset is described in Itkin et al. (2023). In this paper, we use a subsection of the following standard transects (see also Figure 3):

- **Nloop** in the Fortress area of the CO ~~lied~~ was located on deformed SYI. Most Nloop ridges are among the oldest in the CO, with some potentially multiyear. The loop includes crossings of six large old ridges and four small new ridges formed in April 2020.
- **Sloop** ~~lied~~ was located in a relatively flat SYI area with refrozen melt-through ponds. It includes four ridge crossings, one formed in October and three in November 2019.

– **MeltMix** (also referred to as "transect" in Itkin et al. (2023)) was confined to the area that remained accessible for ground surveying in June and July 2020. It covered mixed ice types with twelve ridge crossings of various ages, including two ridges also present on the Nloop.

3 Results and discussion

3.1 MOSAiC Ridge Observatory — EMI point measurements

We now compare the co-located ~~snow freeboard, draft, and~~ drill-hole data ~~from Section 2.7~~ with the EMI retrievals from individual channels ~~.~~ (Figure 5~~shows this comparison for total ridge thickness and CL thickness measured in drill holes alongside the corresponding EMI values (see also Figures A3–A14 in the Supplementary Material~~). To simplify the comparison and avoid additional errors from the often unknown local freeboard, we ~~define the~~ compare CL* instead of CL in this section~~as the distance between the ice surface and the bottom of the layer. Elsewhere in the paper, the CL follows the definition in the introduction—the distance between the waterline and the bottom of the CL.~~. Figures A3–A14 in the Supplementary Material show profiles of EMI retrievals for all the channels on all of the survey dates.

While the data show substantial scatter, the total ridge thickness aligns best with the in-phase channels of the lower frequencies (1.5, 55.3, and 18 kHz). ~~The linear determination coefficient R^2 for the mean of these channels is 0.63 (statistically significant at the 99% confidence level).~~ This is represented by equation:

$$z_{iw} \approx \frac{1}{n}\sum_{i=1}^{n} H_{\text{in-phase}}(f_i), \tag{2}$$

where

$$f_i \in \{1.5, 5.3, 18\} \text{ kHz}.$$

On Allie's Ridge, we exclude two cases where the 1.5 kHz retrieval exceeds 10 m (unlike the other channels) from the figure and correlation analysis. Then the coefficient of determination R^2 for the mean of these channels is 0.63 (statistically significant at the 99% confidence level).

Conversely, the ~~CL~~ CL* thickness aligns mainly with the quadrature values of the highest frequencies (18, ~~60, and 98~~63, and 93 kHz)~~, for which~~ . This is represented by equation:

$$z_{cf*} \approx \frac{1}{n}\sum_{i=1}^{n} H_{\text{quadrature}}(f_i), \tag{3}$$

where

$$f_i \in \{18, 63, 93\} \text{ kHz}.$$

Here the mean yields $R^2 = 0.48$ (also significant at the 99% level). For both linear fits, EMI overestimates low values (level ice), forcing the linear model to underestimate high values, even though the high values follow the 1:1 line well. Drill-hole

measurements also carry a known bias toward larger values due to delayed interface detection during drilling (Høyland, 2002) and under-detection of voids smaller than 0.1 m (Marchenko, 2022).

Additional scatter arises naturally from the footprint mismatch and strong horizontal variability in ridge geometry. Drill holes provide point measurements, whereas EMI footprints span 4–30 m when applying the Reid and Vrbancich (2004) approximation of four times the total ice thickness. This large footprint smooths steep thickness gradients, a known issue that causes underestimation of peak ridge thickness (Pfaffling et al., 2007), although the average ridge thickness along a profile remains realistic (Hendricks, 2009).

Based on drill-hole data, the estimated rubble ~~macro-porosity~~ porosity for these six ridge transects ranges from ~~0.2 to 0.3~~20% to 30% (Salganik et al., 2023d). This suggests that such a level of porosity (or conductivity) is required for the quadrature of high frequencies to detect the bottom of the ~~CL~~CL*. These values are much lower than the porosity of loose platelet ice layers typical for Antarctic sea ice (Hoppmann et al., 2020). EMI sounding clearly depends on the difference in average conductivity (bulk rubble and keel porosity) determined by mean conditions across multiple blocks and voids or by generally soft and wet ice, and it cannot resolve individual voids.

A systematic limitation of the EMI data, beyond the empirical model used here and demonstrated by forward modeling (Neudert et al., 2024), is that individual channels cannot perfectly capture either total thickness or ~~CL~~ CL* (and conversely also CL) thickness. The relatively short and weak GEM-2 transmitter-receiver antenna may also have limited sensitivity to the rubble–seawater interface in thick, highly conductive keels. Furthermore, Figures A3 and A7 show that the in-phase signals of the lower frequencies are affected by metallic objects installed on the Installation transect of Fort Ridge and the Central transect of Allie's Ridge (buoys described in Section 2.4), producing erroneous data at a few locations. Finally, the March–May ridge transects performed by sled are of lower quality, as discussed in the next section.

We argue that our limited point data, combined with a simple linear fit model, provide a valuable first-order approximation of total ridge thickness and ~~CL thickness. Here~~CL* (and CL) thickness. Hereafter, we use the means of low-frequency in-phase channels and high-frequency quadrature channels, as described above, to analyze the seasonal development of ridge consolidation. The same data shown in Figure 5 are presented as ridge profiles in Figure 6, where individual point EMI and snow-depth measurements are connected into six ridge cross-sections. To corroborate our approach, we extract ALS snow freeboard and MB sonar drafts for these profiles (Section 2.7), providing continuous constraints on the upper and lower boundaries of the ridges.

The three EMI profiles across Fort Ridge indicate a maximum keel ~~thickness~~ depth slightly over 6 m, with most of the keel near 4 m draft. At the Installation transect (Figure 6a), we repeated the survey only once. During this second survey, several instruments with large metallic components were already installed, interfering with the EMI signal. This interference appears as abrupt, unlikely decreases in total ridge thickness at those locations (see also Figures A3 and A7). At the Coring transect (Figure 6b), we observe more uniform increases in level ice thickness, CL thickness, and total ridge thickness. At the Optical transect (Figure 6c), discrepancies arise between drill-hole, EMI, and MB sonar measurements at 20–30 m distance. This area exhibits large variability and steep draft gradients. In addition, the drill holes likely contain voids exceeding 1 m at the bottom

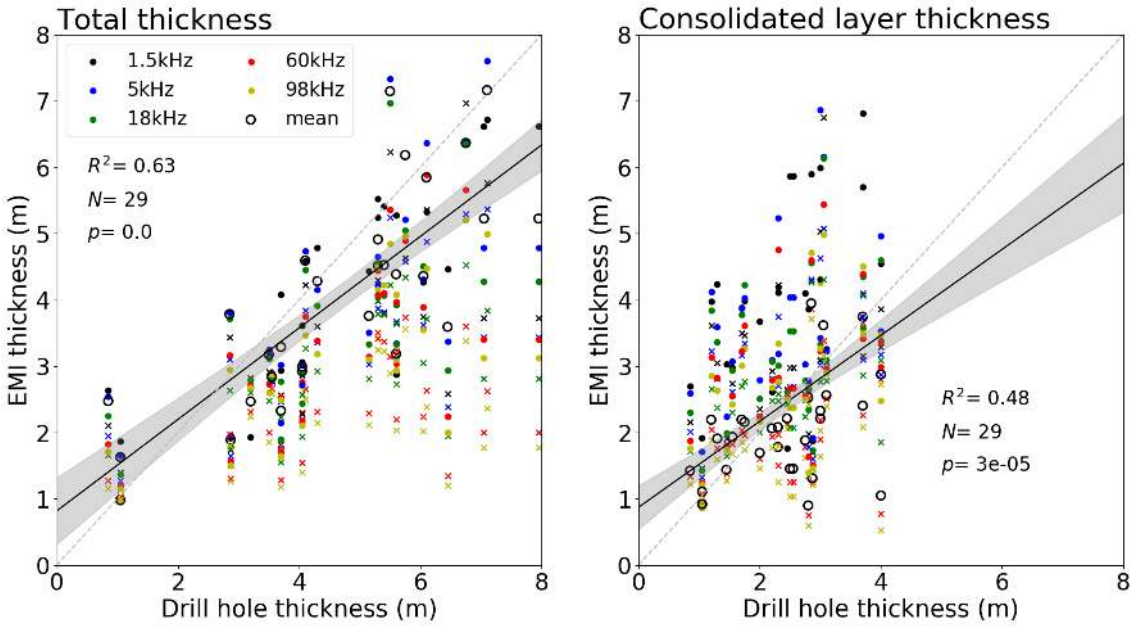


Figure 5. Comparison of a) total ridge thickness and b) consolidated layer (CL*) ridge thickness measured in the winter drill holes and EMI ridge transects. The values of in-phase channels are represented by dots and quadrature channels are represented by crosses. The ~~mean is~~ means represented by circles are calculated only from selected channels (in-phase channels of 1.5 kHz, ~~5~~ 5.3 kHz, and 18 kHz for total thickness and quadrature of 18 kHz, ~~60~~ 63 kHz, and ~~98~~ 93 kHz channels for CL*). The linear fit for these means is a solid black line (both statistically significant at 99% confidence level) with shaded area showing the standard error envelope. The dashed black line shows an ideal linear fit.

(as deployed equipment was not visible in subsequent ROV dives), resulting in porosity ~~beyond~~ above the EMI detection limit and underestimation of total thickness.

The three EMI profiles across Allie's Ridge (Figure 6d–f) indicate a maximum keel ~~thickness~~ depth over 12 m, with a substantial portion of the keel near 6 m draft. Winter drill holes at the keel show substantially lower thickness ~~, but this discrepancy cannot be resolved due to the absence of MB sonar data for Allie's Ridge. All three transects show a gradual decrease in total thickness of the thickest keel section. Some summer drill holes on the lead flank likewise lose about 2 m of ice, consistent with this trend. Drill-hole data reveal large spatial variability at the ridge sail crest, including a "hollow keel" on the Northern transect. As at the Optical transect of Fort Ridge, porosity may exceed the EMI detection limit for total thickness, but no MB sonar data are available to confirm this~~ and thicker flanks. This abrupt thickness gradient in the drill holes is not captured by the EMI method that has a footprint of approximately 30–40 m on this thick ridge. All three transects show a gradual deepening of the CL at the thinner flank, while total ridge thickness decreases. During winter, part of the thickest keel flank erodes (at around distance 20 m), and by July the entire ridge keel erodes to CL depth. Summer drill holes in the Southern

transect still contain water-filled voids within the CL, which EMI does not detect. This under-detection likely results from fresh meltwater in the keel (Salganik et al., 2023d; Lange et al., 2023), which has lower conductivity than sea ice.

A common feature across all transects is that the topographically protected, unconsolidated flanks consolidate the most. The thickness of the unconsolidated layer does not correlate with total ridge thickness—the thickest unconsolidated layers often occur on the flanks, typically near the thinner ice from which the ridge formed. Our transects do not cross the tallest sails or deepest keels. Figure 4 provides a clear visual example of spatial variation in ridge sail elevation and keel depth, which likely drives variation in ridge structure and processes. Strub-Klein and Sudom (2012) report 30–60% variation in CL thickness within a single ridge.

We also compare the ALS and hydrostatic freeboard data shown in Figure 6, both freeboards including snow. This comparison provides insight into ridge buoyancy, which is important for estimating ice thickness from freeboard (e.g., Landy et al., 2020) and for understanding floe-scale processes related to snow loading and ice buoyancy, such as flooding and snow–ice formation (Provost et al., 2017; Merkouriadi et al., 2020). We adjust ALS freeboards to the water level in the drill holes, as described in Section 2.7, while retaining the original relative elevation differences between level ice and ridge sails. We calculate hydrostatic-equilibrium freeboard from sea-ice and snow thickness and densities, using values obtained from snow pits and coring sites ~~(Itkin and Liston, 2024; Salganik et al., 2023c)~~(Itkin and Liston, 2025; Salganik et al., 2023c).

At meter-spaced points along the ridge profiles, we observe local discrepancies of up to 1 m between hydrostatic-equilibrium and ALS freeboards. However, averages over the entire ridge (full keel width) agree well for both estimates (Figure 7a). In contrast, maximum ALS freeboards are roughly one-third higher than maximum equilibrium freeboards (Figure 7b). This pattern aligns with airborne EMI studies (Hendricks, 2009), which assume equal ice volume despite underestimating maximum keel depth due to the large (30 m) EMI footprint typical of airborne surveys. In airborne and satellite altimetry, other laser altimeters replace ALS, but their application is analogous.

Our data also show how sail weight and keel buoyancy interact to determine ridge elevation. Although the maximum elevations of both ridges are similar, the mean elevation is much higher for Allie's Ridge, which has a larger (more buoyant) keel and smaller (lighter) sail (higher keel/sail ratio) than Fort Ridge (Figure 7c). The keel/sail width ratios of our ridges range from 1 to 4, within the reported range but below the literature average of ~~6.8 ± 4.6~~ 3.8 ± 1.8 (Strub-Klein and Sudom, 2012). The ratio of maximum keel depth to maximum sail elevation (Figure 7d), ranging from 3.75 to 5, agrees well with the published statistic of 4.3 ± 2.1 (Strub-Klein and Sudom, 2012). The large scatter in our data and the high standard deviations in published sources indicate substantial variability in how ice mass is distributed within ridges. Further analysis of the ROV draft and ALS freeboard is possible for this unique collocated dataset, but beyond the scope of this study.

3.2 MOSAiC Central Observatory - EMI standard transects

In addition to the point-wise EMI data collected at ridge observatories, accompanied by drill holes and MB sonar measurements, we analyze the less precise EMI sled transects to upscale ridge thickness and consolidation to a broader area. Here, the instrument's pitch and roll are uncontrolled, affecting data quality (Reid et al., 2003; Neudert et al., 2024) to an unknown degree. To evaluate data quality, we examine the seasonal development of the retrievals. First, we compile a time sequence of

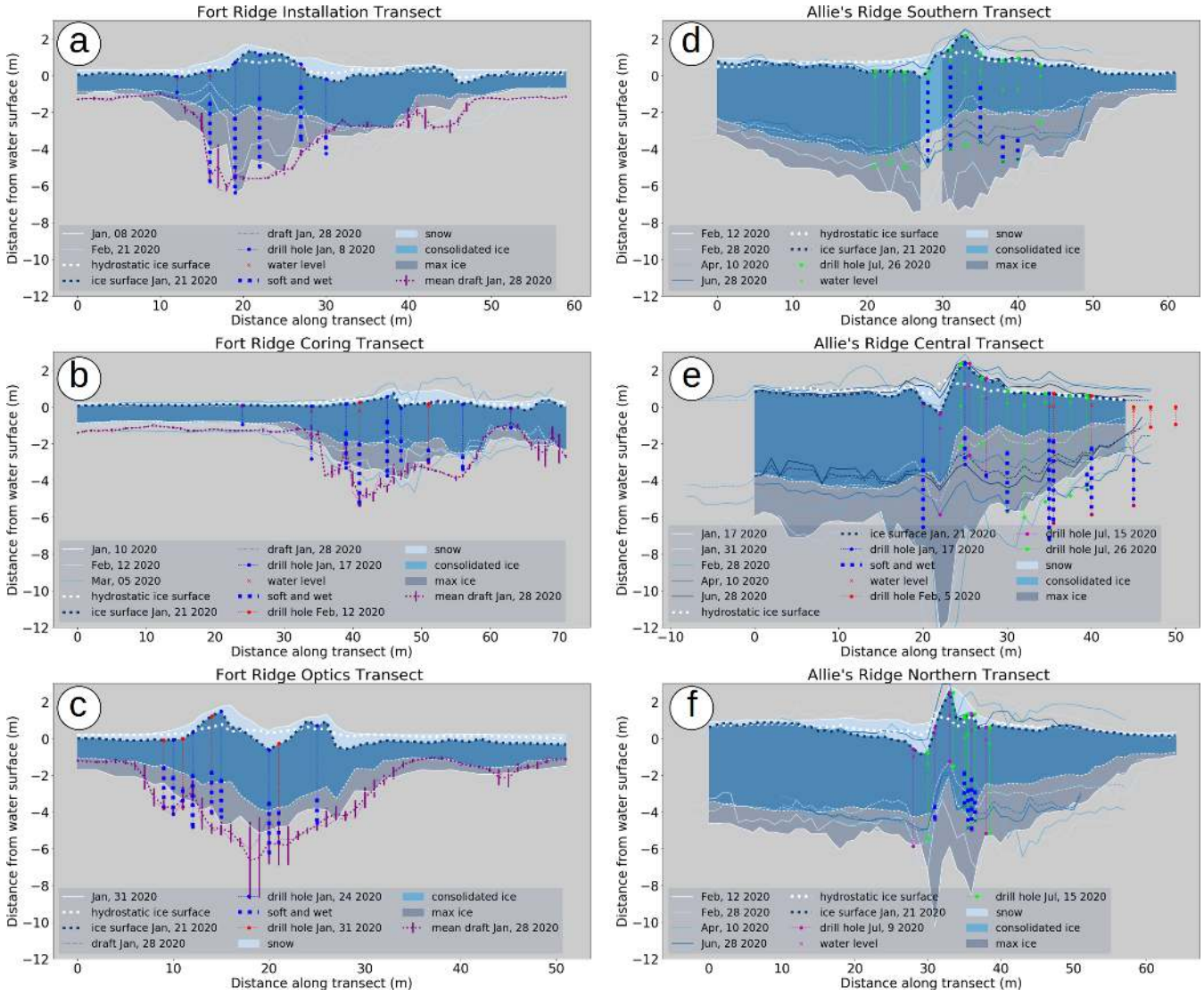


Figure 6. Ridge transects on Fort Ridge and Allie's Ridge for individual EMI survey dates. Solid lines ~~are~~ indicate total thickness, and ~~dash~~ dashed lines ~~are~~ indicate consolidated layer extent. The first date is also shown in color shading, where '~~max~~ sea ice' is CL* 'rubble' is the difference between ~~consolidated layer~~ total thickness and ~~total~~ CL thickness. Individual EMI channel results for these ridge transects are in the Appendix A as Figures A3 to A14.

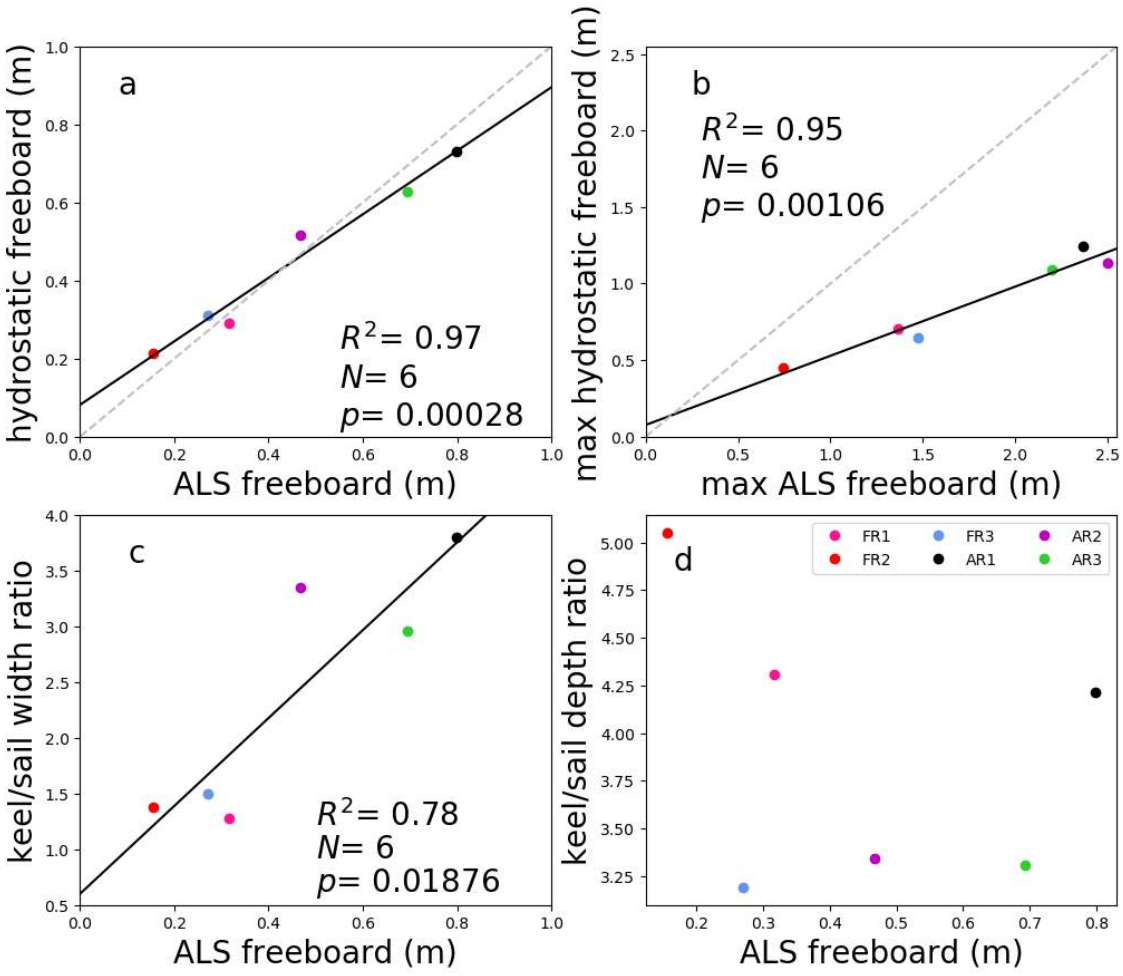


Figure 7. Comparison of a) mean ALS and hydrostatic equilibrium ice freeboards, b) max ALS and hydrostatic equilibrium ice freeboards, c) mean ALS freeboards and keel/sail width ratio, and d) mean ALS freeboards and keel/sail depth/elevation ratio for the ridge transects. The linear determination coefficients R^2 are statistically significant at 99% (for a and b) and at 95% (for c) confidence level - while the number of measurements is low (N=6).

sled-transect maps. For each month from November to July, we select one repeated sled transect (Nloop, Sloop, and/or MeltMix) and include all reconnaissance snowmobile transects. Figure A17 shows these transects and the consolidation fraction (CL-to-keel ~~thickness~~ depth ratio) on the same ALS background as Figure 3b, allowing direct month-by-month comparison of ridge systems (Section 2.9) and consolidation fractions.

For the repeated winter transects, Nloop and Sloop, consolidation increases over the Old, October, and November ridges from November to April. In contrast, the newly formed ridges in April show lower consolidation fractions. The reconnaissance transects extend the dataset, detecting all ridge crossings with consolidation below 100%. The MeltMix transect in June also shows a mix of consolidated and non-consolidated ridges, with the latter originating from the March/April ridge system group.

In July, all ridges appear consolidated, with consolidated and total ice thicknesses closely matching. These measurements are noisy, and CL thickness occasionally exceeds total thickness. This behavior likely results from fresh meltwater accumulating beneath level-ice areas between ridges (Figure A14), with conductivity similar to that of sea ice. As noted by Neudert et al. (2024), overestimated sea-ice salinity can bias consolidated-layer thickness low, especially on inclined surfaces like ridges. Here, however, weekly calibration minimizes sensitivity to seasonal salinity variations. Furthermore, Salganik et al. (2023e) documented ridge keels at ~~melting~~ melting temperatures and Smith et al. (2025) demonstrated that meltwater presence is highly variable, driven by keel melt, snowmelt, level-ice melt, and melt-pond drainage.

The apparent oscillations in CL thickness in June and July (Figure A14) likely result from meltwater layers of different origins, modulated by changes in sea-ice drift speed. MeltMix shows a CL thicker than the total thickness at the end of June and again after July 10, while between these dates the CL appears realistic (i.e., thinner than total thickness). The June meltwater layer may be associated with snowmelt, whereas the July layer likely results from melt-pond drainage combined with low drift speeds, allowing a persistent freshwater layer to form (Salganik et al., 2023e; Smith et al., 2022). This layer, containing platelet ice and false bottoms, developed beneath the ice between July 6–29 (Smith et al., 2022). Drainage channels formed at the end of June, and by late July some ponds lacked a bottom (Webster et al., 2022).

Similarly, meltwater cavities within ridges—whether consolidated or not—remain undetected, as evident from drill holes on Allie's Ridge (Figure 6). During the melt period, keels melt faster than level ice (Amundrud et al., 2006; Shestov et al., 2018; Salganik et al., 2023e; Perovich et al., 2003), because fresh meltwater and false bottoms insulate level ice from ocean heat.

~~Maps of ridge consolidation for sled transects in the CO from a) December, b) January, c) February, d) March, e) April and f) June. The ridges in Sloop (S) and Nloop (N) that were used for time series are marked by a black square. The ALS freeboard map in the background is from 21 January 2020, with identical colormap, extent and orientation as on Figure 3.~~

From the full Nloop and MeltMix transects, we selected a subset crossing the same two neighboring ridges formed in October or earlier. Figure 8a shows thick initial snow and low consolidation until mid-January, followed by simultaneous keel and sail snow erosion, with deposition in the drifts. Between mid-January and mid-March, platelet ice formed at the same location (Katlein et al., 2020). By June, MeltMix data over the same ridge (Figure 8b) indicate that the ridge simply erodes to the consolidation layer, explaining why full consolidation occurs rather than freezing of the CL.

From the full Sloop transect, we selected a subsection over a ridge formed in November (Figure 8c). The ridge consolidated during winter, but consolidation slowed as snow accumulated. Most winter consolidation occurred between December and

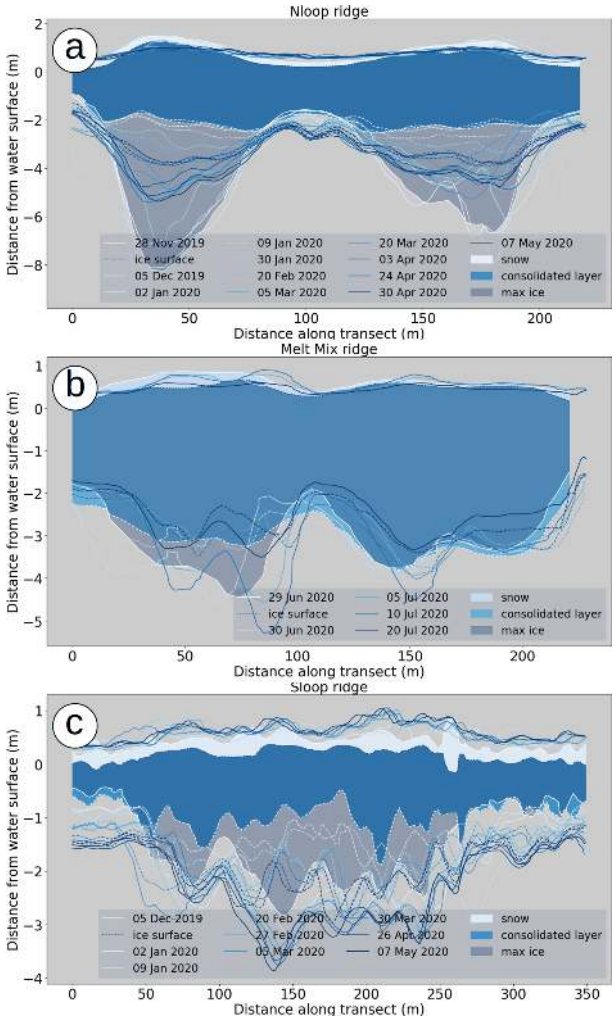


Figure 8. Selected subsections of a) Nloop, b) MeltMix, and c) Sloop transects over ridges. The two ridges in Nloop are the same as in the MeltMix. Solid lines ~~are~~ indicate total thickness, and ~~dash~~ dashed lines ~~are~~ indicate consolidated layer extent. The first date is also shown in color shading, where 'max ice' is the difference between ~~consolidated layer~~ total thickness and ~~total~~ consolidated layer thickness.

February. This ridge had a high sail, similar to Nloop ridges, so EMI roll error was comparable. However, no keel erosion occurred in this relatively shallow keel.

470 The results of this section show that sled transects produce results comparable to point transects. Sled data detect all ridges as having decreased CL compared to level ice. All ridges also exhibit a temporal progression in consolidation, with similarly aged ridges consolidating at similar rates, suggesting that the transect crossings are representative of the ridge systems. Given the EMI positive bias caused by antenna roll and pitch (Neudert et al., 2024; Reid et al., 2003), sled-transect data become more reliable once ridge sails are less steep due to snow drifts at their flanks.

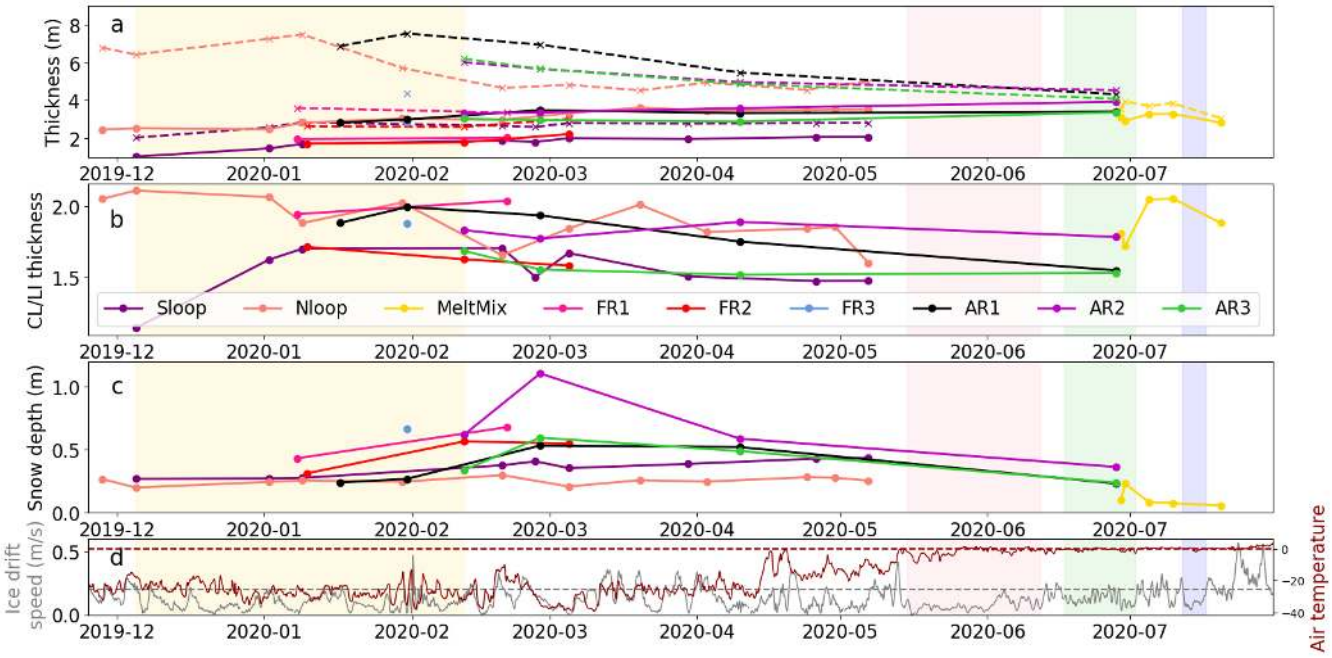


Figure 9. Time series of average values from individual ridge transects at Fort Ridge (FR1–3), Allie's Ridge (AR1–3), Nloop, Sloop and MeltMix. Periods with low drift speeds (typically under 0.2 m s^{-1}) are shaded by colors. a) Total ridge thickness (~~dash~~ dashed line and crosses) and consolidated layer thickness (circles and full lines), b) ratio of consolidated layer (CL) and level ice (LI) thickness, c) average snow depth on ridges, and d) sea ice drift speed and air temperature.

3.3 Seasonal time series

Because measurements over individual ridges in the previous sections—by point measurements (6 transects, Figure 6) and sled measurements (the three largest ridges, Figure 8)—were repeated, we can track the seasonal development of their mean properties. Each analyzed ridge represents one of the ridge system groups defined in Section 2.9: Old ridges are represented by Nloop ridges, October ridges by Fort Ridge, November ridges by the Sloop ridge, and January–February ridges by Allie's Ridge. As the CO set-up changed between May and June, none of the March–April ridges were revisited.

Figure 9a shows total and CL thicknesses of the ridges. For ridges with deep keels (Allie's Ridge and Nloop), total thickness decreases over time, while for shallow-keel ridges (Fort Ridge and Sloop) it remains stable. Deep-keel ridges have thicker CLs than shallow ridges, regardless of formation time. CL thickness increases gradually: for shallow ridges from ~~approximately~~ 1 m to 2 m, and for deep ridges from 2 m to 3 m. For both ridge types, CL and total thickness converge and become similar by June and July.

To assess the realism of these CL developments, we compare them to surrounding level ice thickness, summarized from historical data in Figure 2b. We estimated level ice thickness visually, by identifying the thinnest sea ice of the thickest ice type near the ridge. For example, for Allie's Ridge, we used level ice on the second-year ice side, not the lead. The ratio of CL to

level ice thickness, estimated from our data (Figure 9b), approaches the theoretical winter limit of 1.8 (Leppäranta and Hakala, 1992) and slightly exceeds it for deep ridges. Initially, the ratio varies between 1.6 and 2, then decreases slowly after March. This pattern may reflect a peculiarity of the MOSAiC dataset, where ridge snow depth (Figure 9c) reached more than twice the level ice depth, which remained below 0.2 m for most of the winter (Itkin et al., 2023). The relatively thick snow likely slowed ridge consolidation compared to the faster growth of level ice.

The EMI-based findings can be compared to consolidation detected by thermistor chains at Fort Ridge and Allie's Ridge as shown in Figure 10a,c. Initially, CL thickness is 1–1.5 m for Fort Ridge and 1–2 m for Allie's Ridge, lower than EMI estimates. In some cases, these differences decrease abruptly due to rapid consolidation, as discussed by Salganik et al. (2023d). Part of the discrepancy likely originates from EMI (and drill hole) overestimation, as described in Section 3.1. EMI likely cannot detect small voids because of its large footprint and limited sensitivity to minor conductivity changes. Thermistor chains are point measurements, deliberately deployed in drill holes with the thinnest CL, highest rubble porosity, and most voids to monitor consolidation. For example, Allie's Ridge drill-hole ~~porosity estimates are~~ rubble porosity was 29±15% (~~typical, Figure 2a~~mean ± standard deviation), whereas thermistor-chain ~~measurements give~~ estimates at selected highly porous locations were 43–46%.

We ~~can further assess the realism of consolidation detected by EMI and thermistor chains using a 1-D thermodynamic model~~ further compare the observed CL growth rates with thermodynamic model predictions. The model accounts for atmospheric thermodynamic forcing influenced by snow cover at individual MOSAiC point transects. It does not include rapid consolidation mechanisms such as platelet ice formation (Katlein et al., 2020) or integration of snow slush and meltwater into voids (Salganik et al., 2023d). We initialized the model ~~with EMI~~ using EMI-derived CL thickness and ~~by~~ observed snow depth, ~~using~~ with the mean and standard deviation of CL thickness calculated from the central parts of the transects shown in ~~Figures~~Figure 6.

Model simulations show 0.6–1.0 m consolidation (CL thickness increase) for the three Allie's Ridge transects, compared to 0.4–0.6 m from EMI (Figure 10a–c). Two thermistor chains recorded 0.4 m consolidation at the ridge flank and 2.8 m at the ridge interior, with rapid ice growth in April and May. For Fort Ridge, EMI indicates 0.1–0.3 m consolidation, the model estimates 0.3–0.5 m, and thermistor chains measure 0.4–1.0 m (Figure 10d–e).

Faster consolidation from thermistor chain measurements generally reflects the much thinner initial CL thickness (Figure 10a,d). When consolidation starts at ridge formation with zero initial thickness (not shown), the thermodynamic model predicts CL growth similar to IMB estimates, reaching 1–2 m in January, substantially thinner than EMI values. These simulations cannot reproduce rapid consolidation events~~, and the general agreement between EMI and the model indicates that such rapid events are local~~. The agreement between modeled and EMI-derived CL growth suggests that the rapid consolidation observed by individual thermistor chains is spatially localized.

EMI-based estimates of keel ~~draft~~ depth for deep-keel ridges (Allie's Ridge and Nloop) ~~reveal substantial~~ indicate substantial local winter–spring ~~melt~~ keel thinning of 1–3 m (Figure 9a)~~, with the strongest reduction occurring after mid-February, coinciding with increased sea-ice drift speed (yellow shading in Figure 9d). For Nloop, part of this apparent "keel disappearance" likely reflects reduced pitch-related overestimation Reid et al. (2003) as snow accumulated. In contrast, Allie's Ridge data, collected with a horizontal antenna, still show melt exceeding~~ . This exceeds the reduction measured in the drill-hole~~measurements,~~

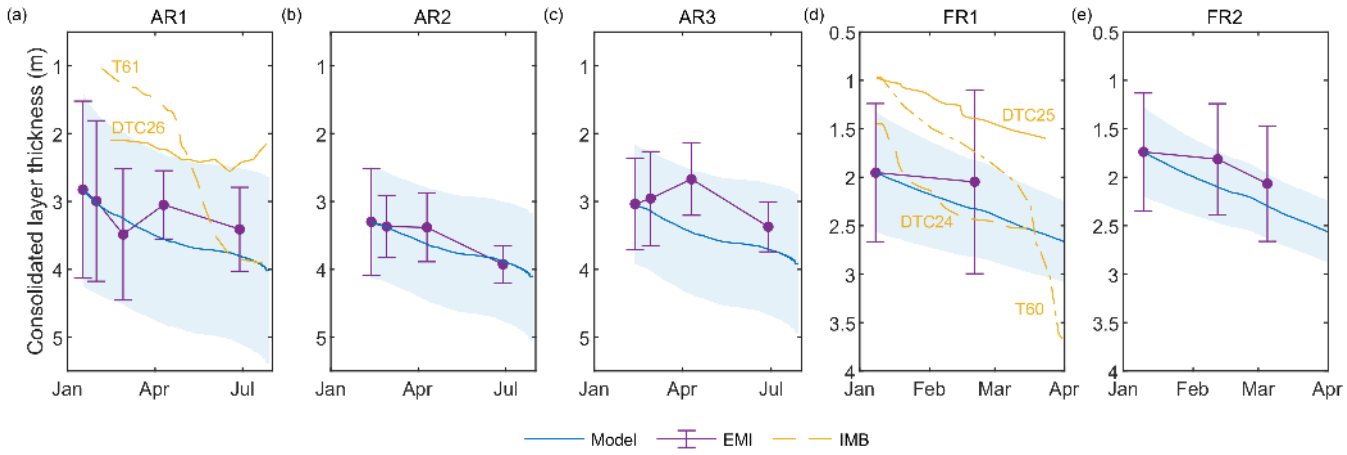


Figure 10. Temporal evolution of consolidated layer thickness from 1-D thermodynamic modeling (blue line is mean and blue shading is one standard deviation from all transect points), EMI measurements (purple dots for means and whiskers for one standard deviation), and individual IMBs (yellow lines).

~~which recorded~~ , where only a 0.9 m draft reduction from January to July ~~Salganik et al. (2023d). Such pronounced wintermelt was never observed before, but typically only shallow ridges are sampled. For example, Guzenko et al. (2025) reported spring draft reductions of 0–0.4 m for ridges with average drafts of 2.8~~was recorded. During winter, ridges may slowly melt, with melt rate defined by the value of the ocean heat flux, which was 1–3 W m^{-2} (1–3 cm $month^{-1}$) during November~~–3.8~~May based on MOSAiC oceanographic measurements (Schulz et al., 2024). Thermistor-chain measurements at the same ridge indicated less than 0.02 m ~~. Moored sonar statistics provide limited insight into winter–spring melt, as they cannot reliably separate newly formed and older ridges. Since melt rates scale strongly with keel draft Amundrud et al. (2006); Salganik et al. (2023e) , these observations highlight that the seasonal evolution of large ridges remains poorly constrained.~~ of keel melt before June (Salganik et al., 2023d). The keels at the Fort Ridge, where some MB sonar draft measurements are available, did not thin. We therefore assume that the apparent thinning of deep keels is an artifact connected to the empirical calibration of the EMI signals over level ice. The values there, especially the beginning of the season, did not exceed 4 m, and the resulting EMI estimates over deep keels were correspondingly highly uncertain. In the future, we recommend to increase the calibration elevation to be close to the expected maximum distance between sail and keel.

Because the porosity detection by EMI depends on conductivity, there are further discrepancies during the melt period, when low conductivity water appears inside the voids or at the ice undersurface. The voids filled with freshwater can not be detected by EMI. Similarly, the summer CL thickening described in the previous section may reflect meltwater accumulation rather than actual consolidation. Low drift speeds are ~~also~~ crucial for meltwater accumulation between keels. During the melt period, low-drift-speed intervals (pink, green, blue in Figure 9d) coincide with the ~~apparent CL thickening described in the previous section, likely reflecting meltwater accumulation~~transient increases in the CL thickness.

4 Conclusions

This paper provides a comprehensive description of ridges at the MOSAiC CO and an analysis of the EMI data collected there. EMI observations are compared with ridge drillings, surface elevation, draft, thermistor chains, and a 1-D thermodynamic model. Our key findings are:

1. Multi-frequency EMI sounding provides valuable insight into internal ridge structure by distinguishing ~~CL~~ CL* thickness from total ridge thickness. Standard errors of the linear fit range from 5 to 30%, corresponding to approximately 0.2–0.5 m for ridges 6–8 m thick and ~~CL~~ CL* thicknesses of 1–4 m.

2. EMI sounding enables spatially extensive surveys and tracks the seasonal evolution of ridge porosity and thickness. We identified 35 ridge systems formed within the 2 km by 1.5 km area between October 2019 and May 2020. Grouping the EMI transects by formation period shows that these ridges initially had low CL compared to level ice, gradually consolidating to about 80% by May. July data indicate that many ridges were fully consolidated by that time. ~~The deepest ridges likely experienced keel erosion over the winter.~~

3. EMI sounding supports assessment of hydrostatic equilibrium and ridge geometry. For MOSAiC ridges, hydrostatically calculated freeboard agrees with ALS-measured freeboard, although maximum hydrostatic freeboards are about one-third lower. Ridge shape parameters derived during MOSAiC are consistent with literature averages.

4. Multi-frequency EMI data collected during the melt season may detect meltwater layers beneath the ice. Further validation, including direct measurements of meltwater layers, is required.

Our combined ~~dataset—EMI~~dataset—EMI, drill-hole observations, MB sonar measurements, and thermistor-chain ~~records—indicates that the porosity threshold for reliably detecting total ridge thickness by EMI is 20–30%~~ records—suggests that rubble porosity of 20–30% is sufficient for high-frequency quadrature channels to distinguish the consolidated layer from underlying unconsolidated rubble. EMI-derived CL thickness is likely biased high. Point transects provide the highest-quality data, while sled transects (with an inclined antenna) also yield useful results; future surveys should record antenna inclination. We also recommend expanding the range of calibration distances towards expected total thickness of the surveyed ridges. Additional co-located measurements—particularly ALS and MB sonar topography with improved positioning and more thermistor chains—are needed to better quantify systematic biases in EMI-based ridge characterization. We also encourage a follow-up study to expand our preliminary empirical approach by using inverse modeling as in Neudert et al. (2024).

Despite ~~these~~ the limitations, the empirical multi-frequency EMI approach can greatly expand the otherwise scarce ridge measurements (e.g., Figure 2) and guide the selection of ridge study sites, which has often relied solely on sail appearance. Near-real-time processing of multi-frequency EMI measurements ~~could~~ can provide valuable guidance before labor-intensive ridge drilling and coring.

Data availability. All of the transect data used in this study are available in PANGAEA (Itkin et al., 2021; Hendricks et al., 2022). The reprocessed datasets will be published on Zenodo as soon as this paper is accepted. The ice mass balance buoy data can be found in Granskog et al. (2020, 2021); Salganik et al. (2023), the ridge salinity is available in Lange et al. (2022); Salganik et al. (2023b), the ridge density is available in Salganik et al. (2023c), the ridge drilling data can be found in Salganik et al. (2022, 2023a), the multibeam sonar data can be found in Katlein et al. (2022), the snow density data can be found in Macfarlane et al. (2021), the airborne laser scanner measurements can be found in Hutter et al. (2023a), the atmospheric conditions can be found in Cox et al. (2023a).

Code and data availability. The code used for data analysis and plotting is available in https://github.com/loniitkina/tt_tools. The thermodynamical model code is available in https://github.com/esalganik/EMI-consolidation. When the paper publication is finalized, the final combined version of the code will be archived at Zenodo.

1 ~~Appendix A~~

Appendix A

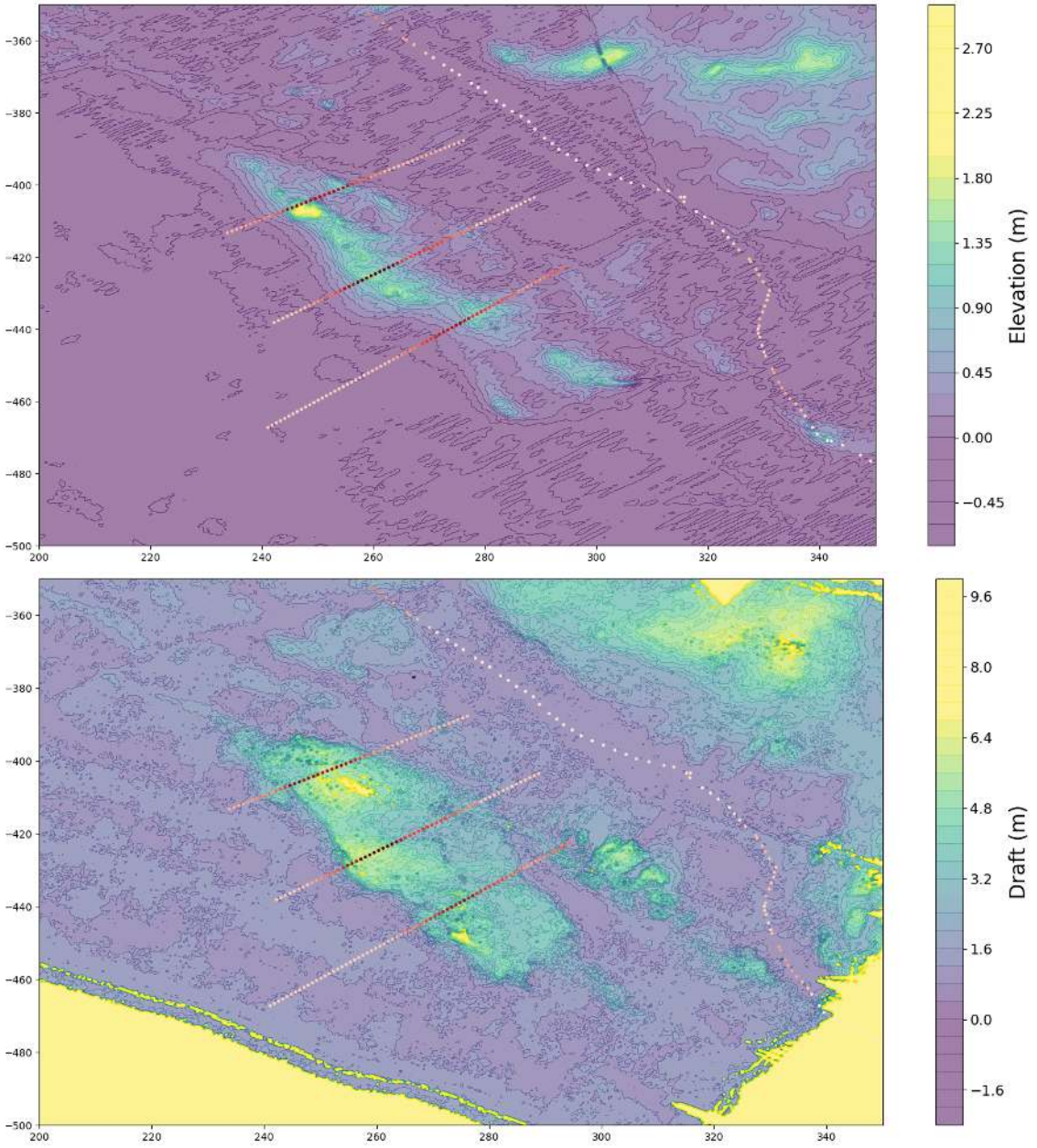


Figure A1. Fort Ridge snow freeboard (top) and draft (bottom) with 3 cross sections from top to bottom: Optics transect, Installation transect and Coring transect. Part of the Nloop transect over level ice is also visible.

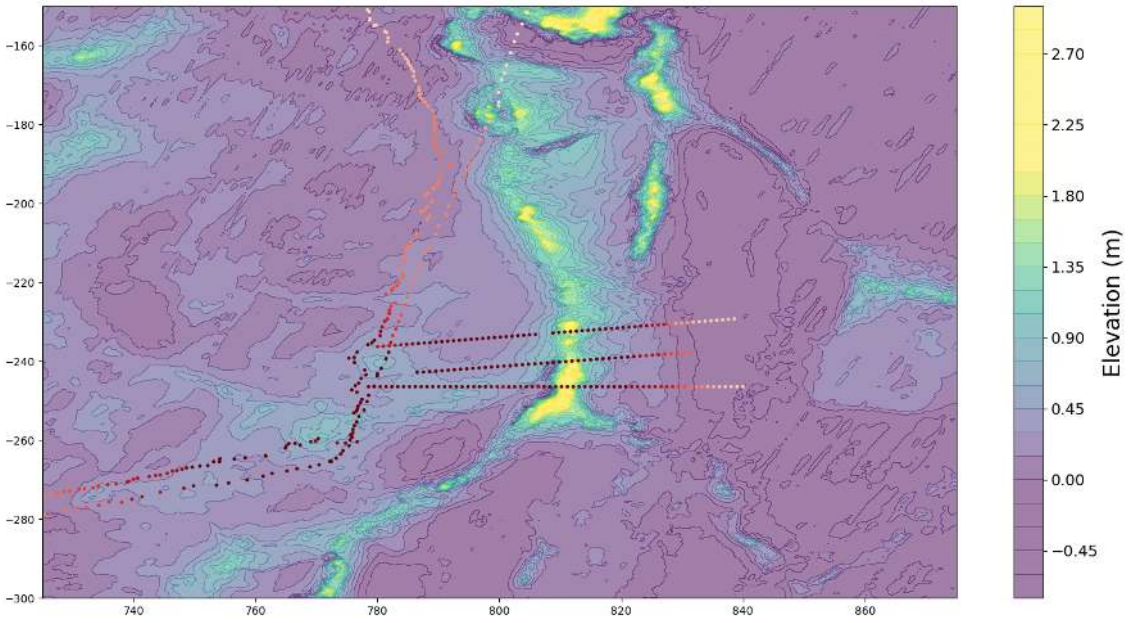


Figure A2. Allie's Ridge snow freeboard with 3 cross sections from top to bottom: Southern transect, Central transect and Northern transect.

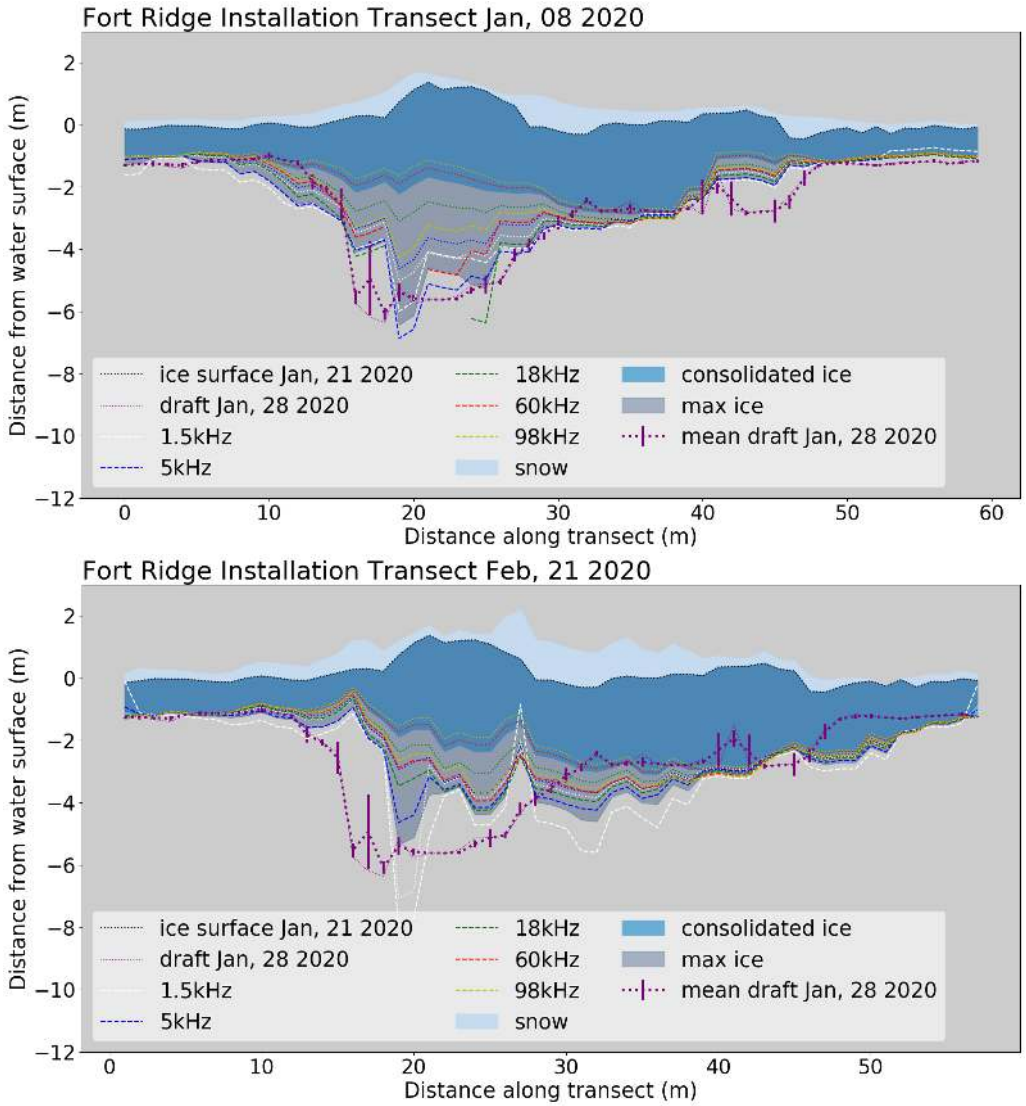


Figure A3. All Fort Ridge Installation transects with all EM channels (in-phase channels are ~~dash~~ dashed lines and quadrature channels are ~~dot~~ dotted lines). Instruments were installed at distances 0, 17, 22, 27 and 55 m after the first transect in January 2020.

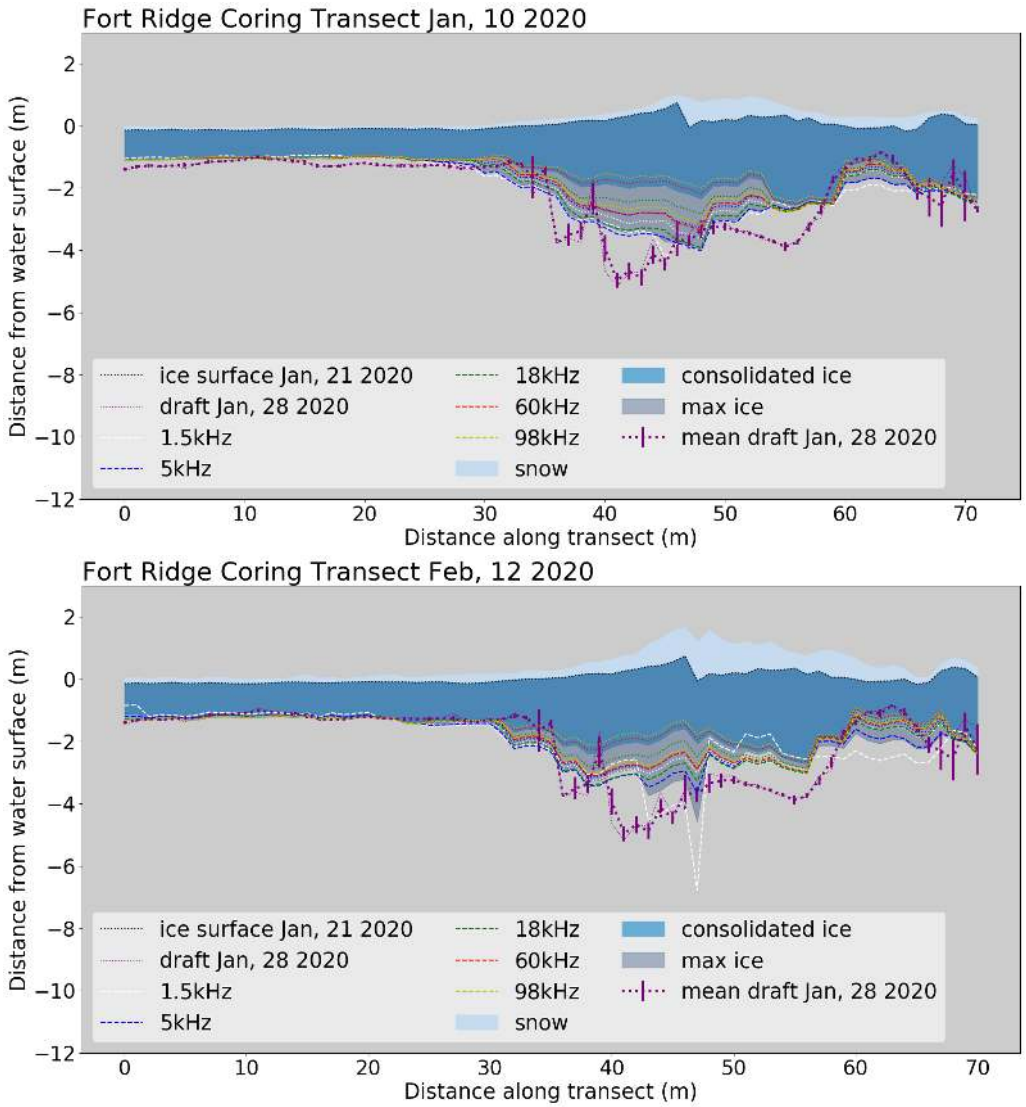


Figure A4. All Fort Ridge Coring transects with all EM channels (in-phase channels are ~~dash~~ dashed lines and quadrature channels are ~~dot~~ dotted lines).

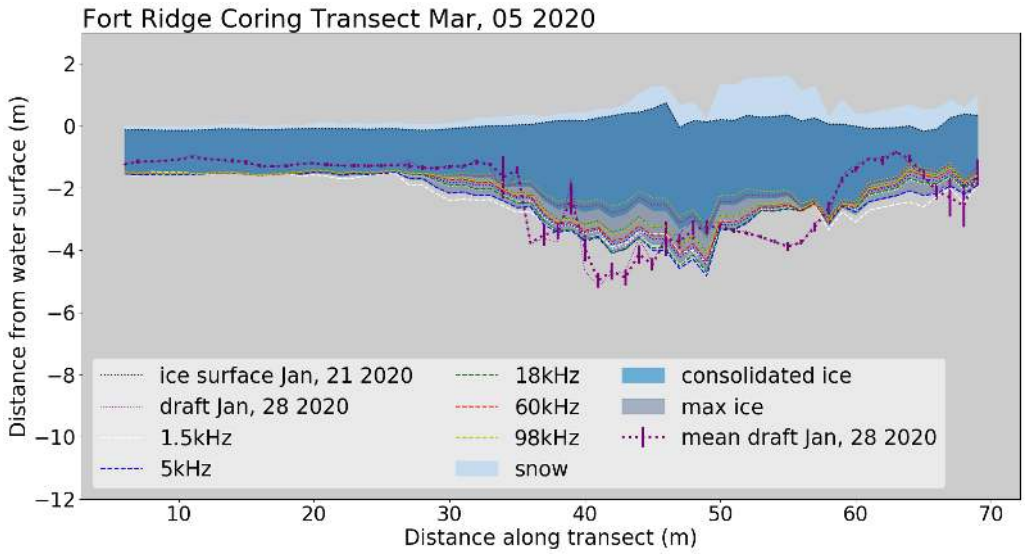


Figure A5. Figure A4 continuation.

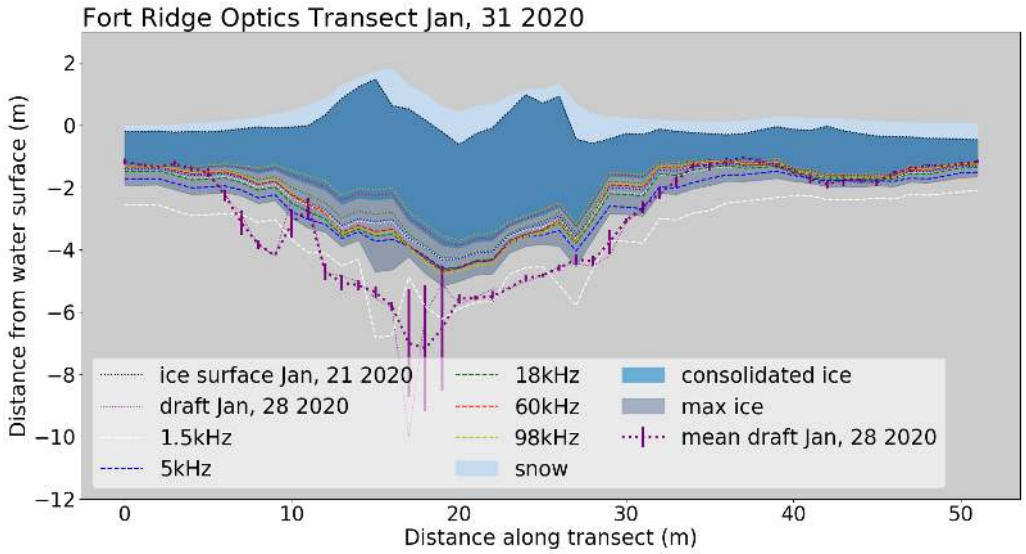


Figure A6. All Fort Ridge Optics transects with all EM channels (in-phase channels are ~~dash~~ dashed lines and quadrature channels are ~~dot~~ dotted lines).

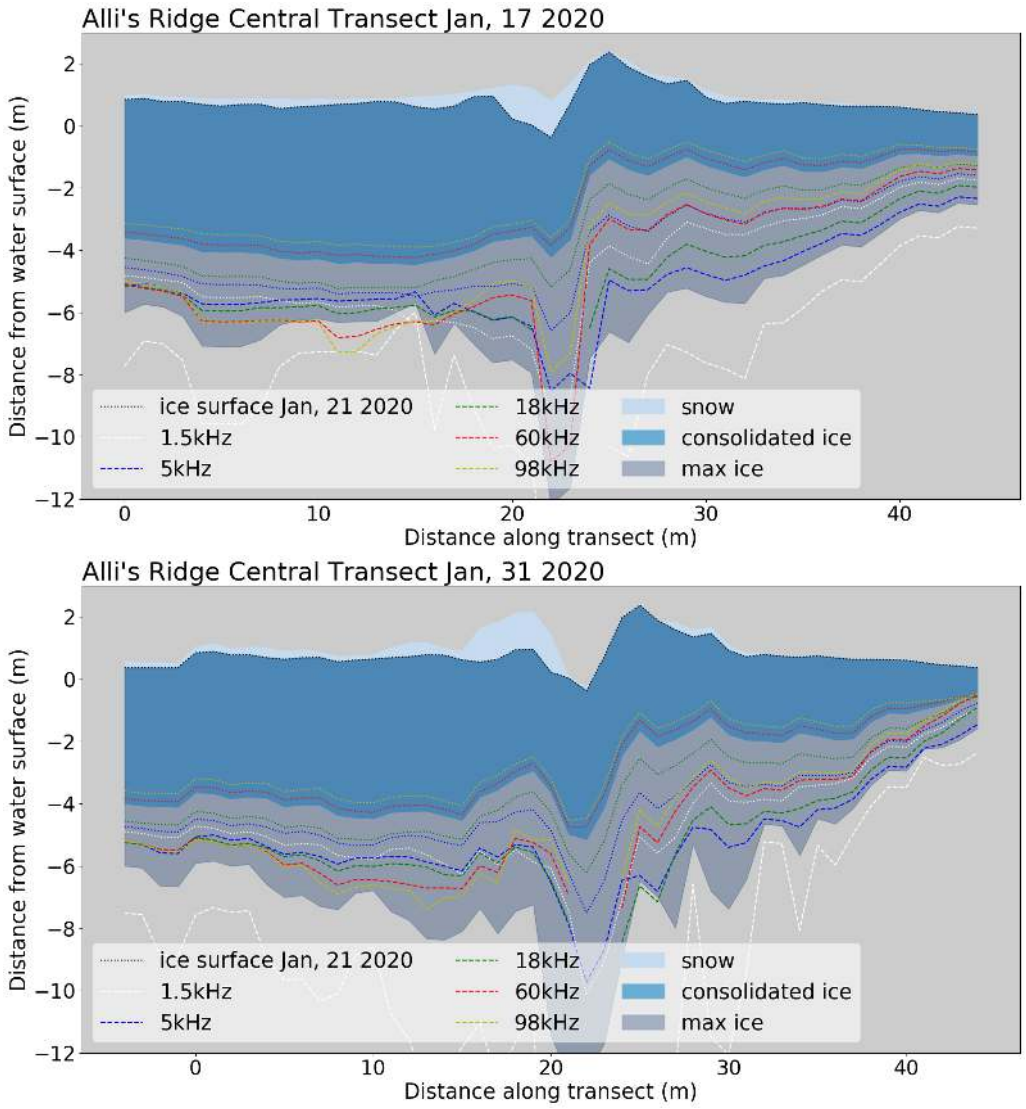


Figure A7. All Central transects of Allie's Ridge ~~Central transects~~ with all EM channels (in-phase channels are ~~dash~~ dashed lines and quadrature channels are ~~dot~~ dotted lines). Instruments were installed at distances 35 and 45 m in February 2020.

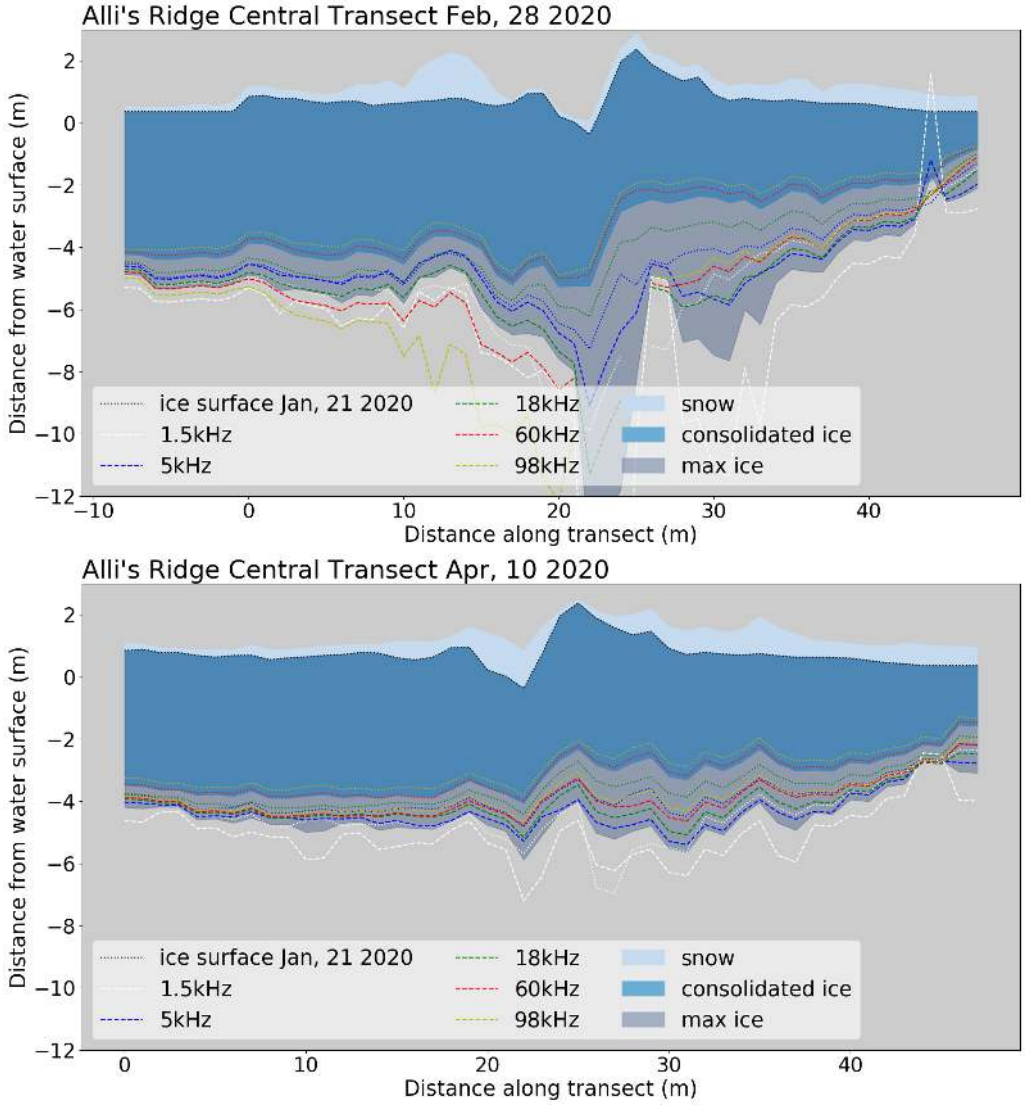


Figure A8. Figure A7 continuation.

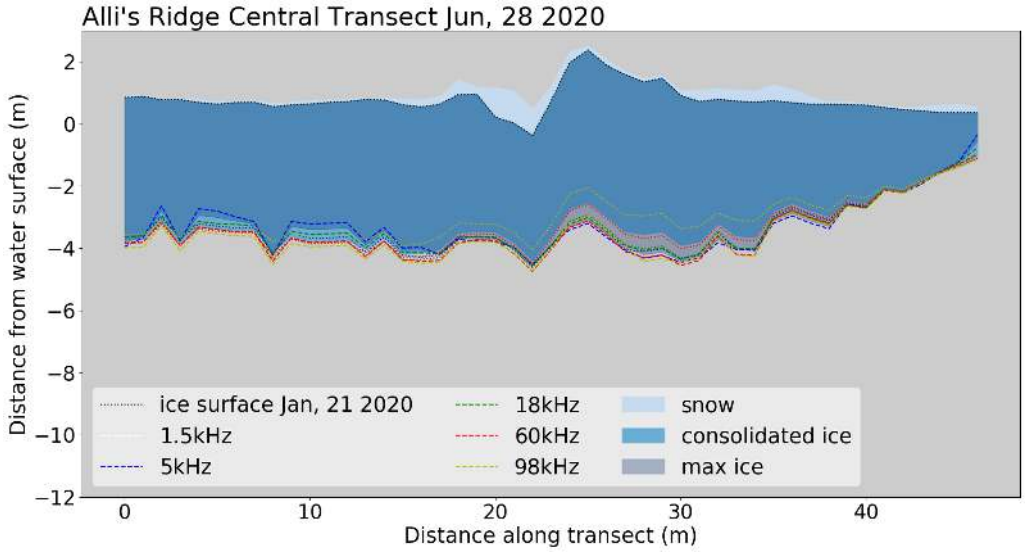


Figure A9. Figure A7 continuation.

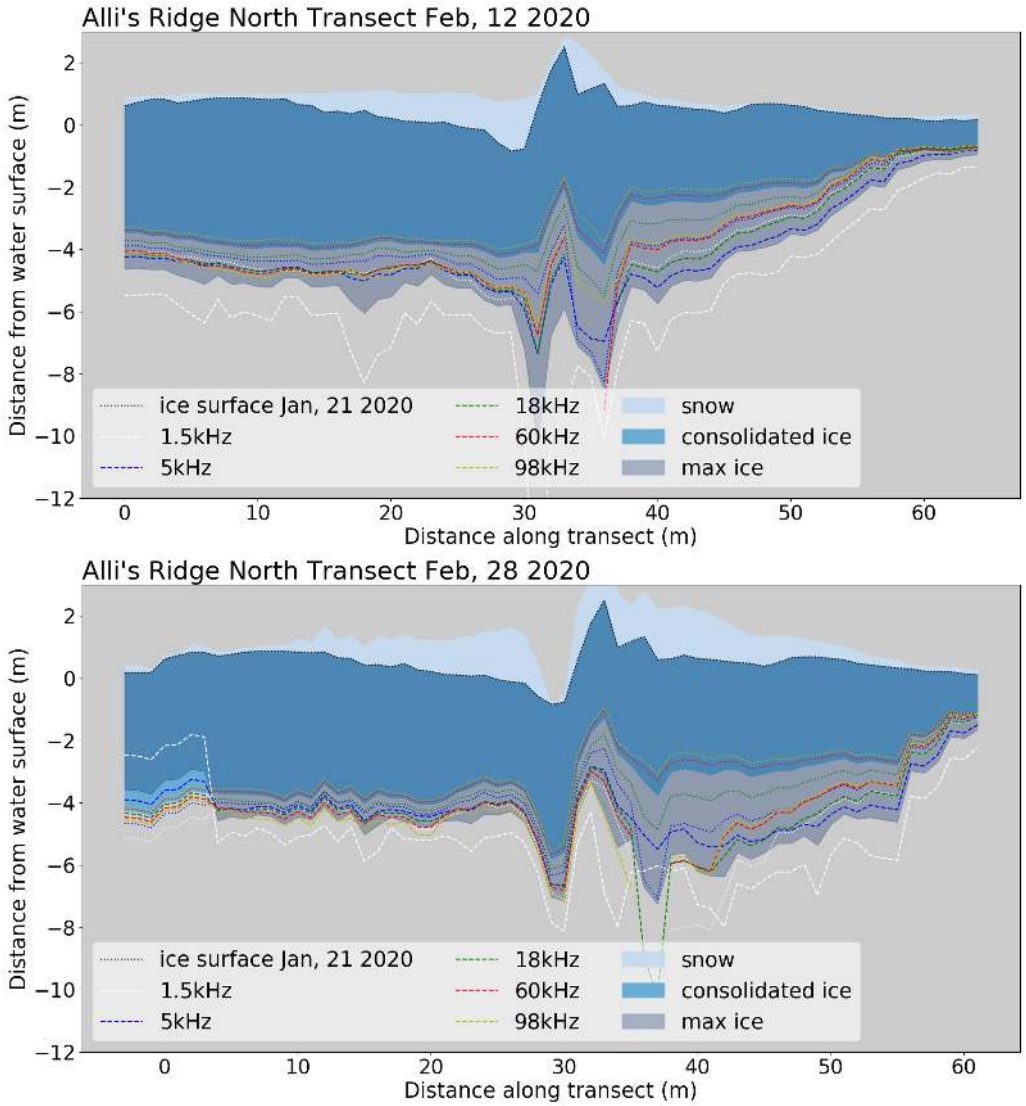


Figure A10. All Allie's Ridge North transects with all EM channels (in-phase channels are ~~dash~~ dashed lines and quadrature channels are ~~dot~~ dotted lines).

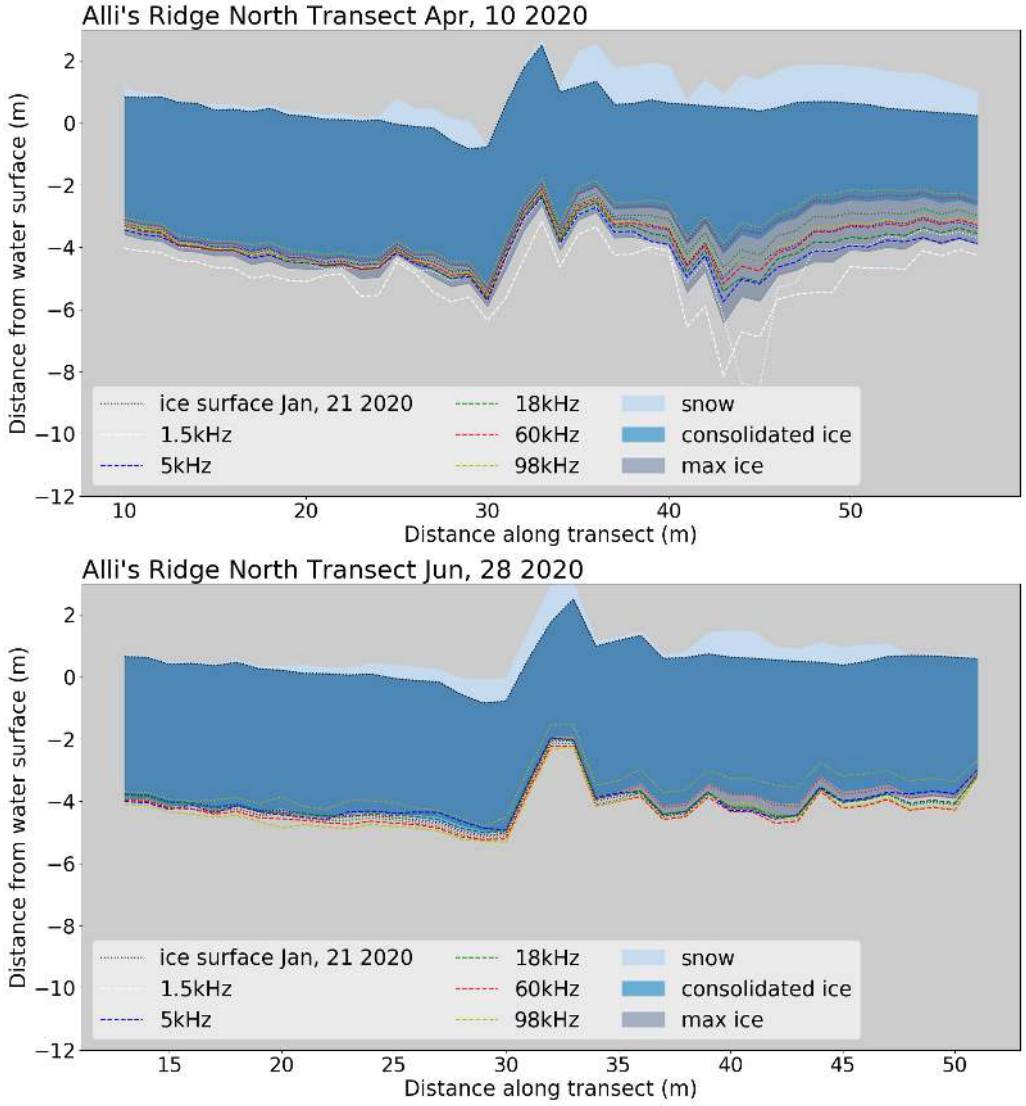


Figure A11. Figure A10 continuation.

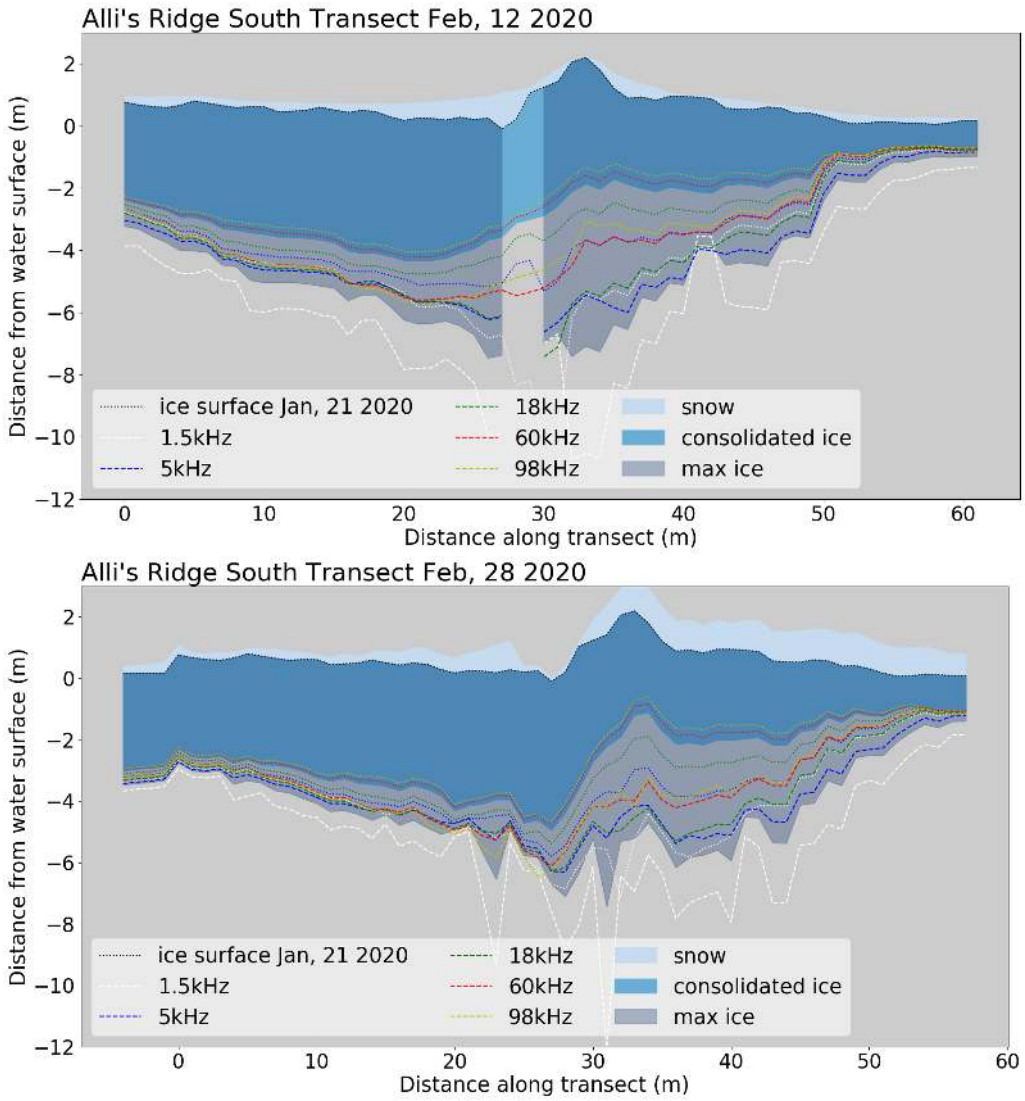


Figure A12. All Allie's Ridge South transects with all EM channels (in-phase channels are ~~dash~~ dashed lines and quadrature channels are ~~dot~~ dotted lines).

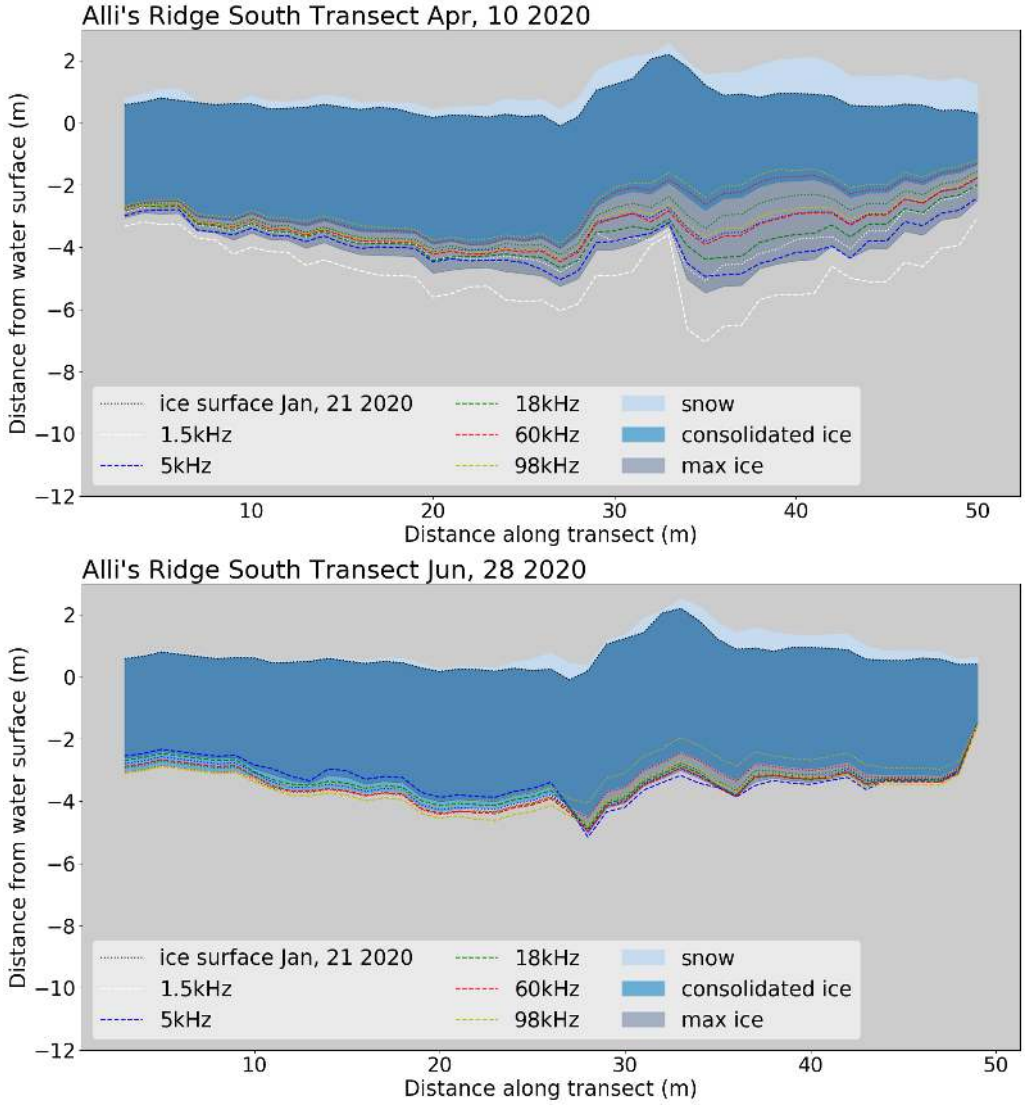


Figure A13. Figure A12 continuation.

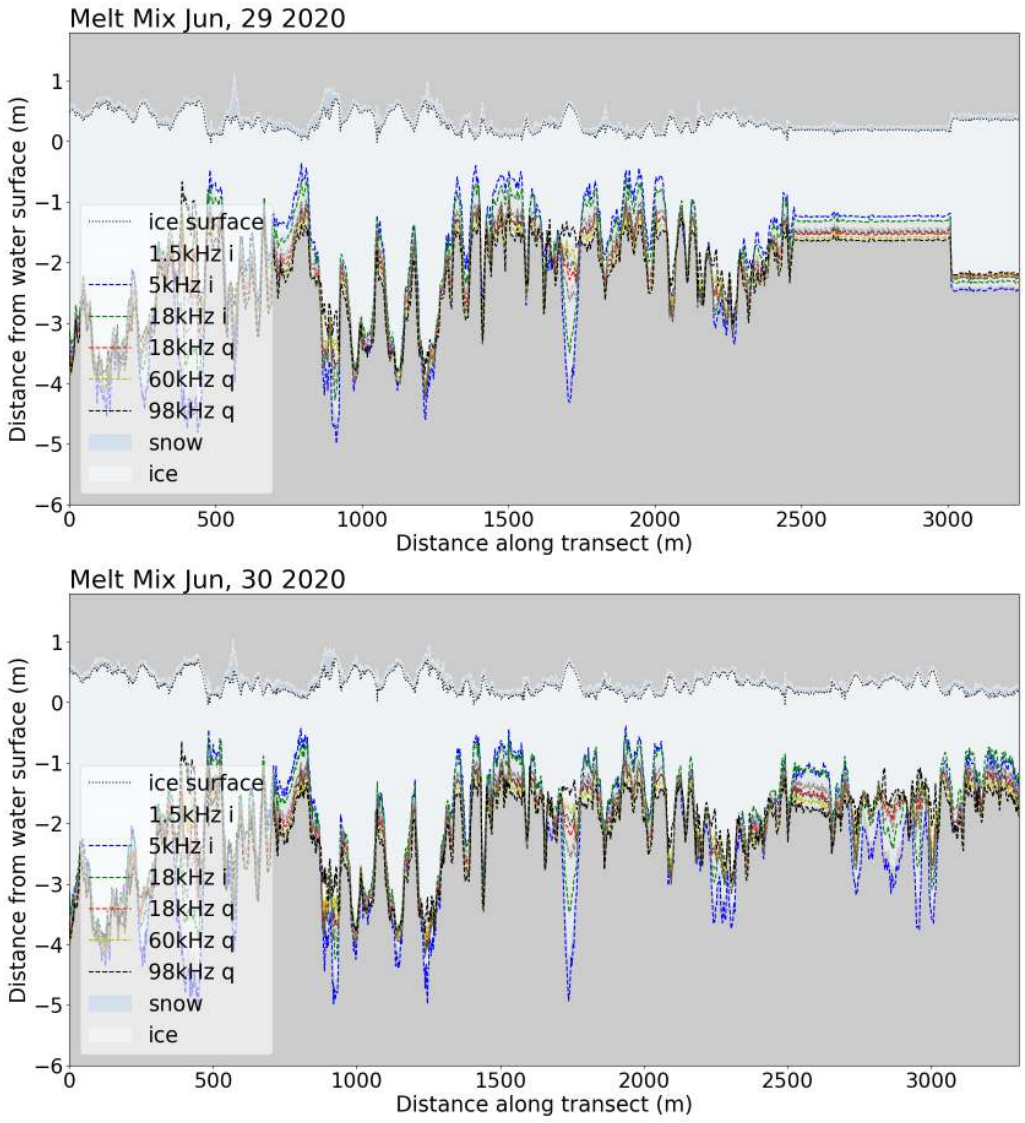


Figure A14. Selected MeltMix sled transects with a selection of EM channels.

Author contributions. PI, DD, CK, IR, AJ, RR, and EvS planned the fieldwork and collected the data. PI and EvS led the data analysis and interpretation, with contributions from all co-authors. MN provided essential guidance on the application of the EMI method. ES contributed key expertise on sea-ice coring, drill-hole measurements, thermistor-chain data, and 1-D modeling. PI wrote the manuscript with input from all co-authors.

Competing interests. The authors have no competing interests.

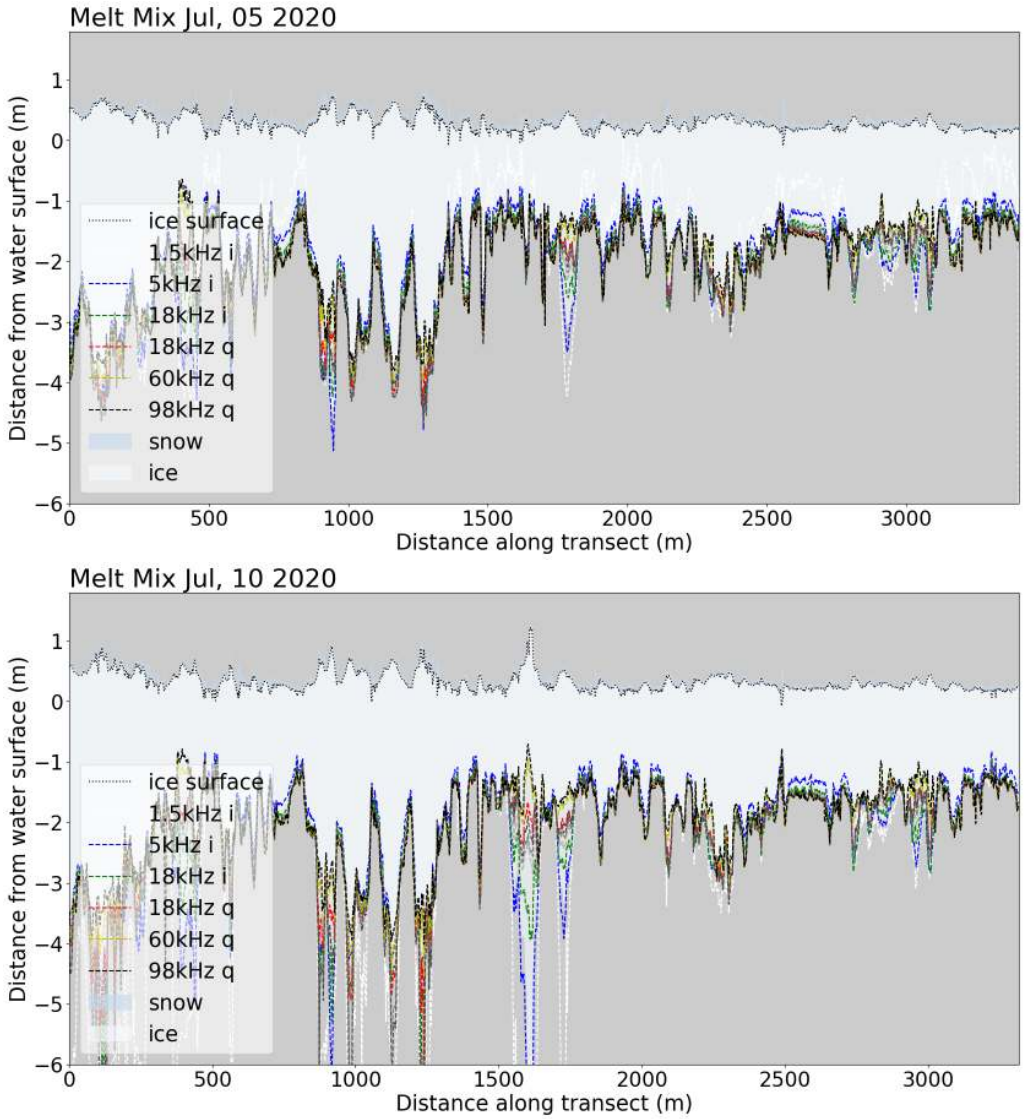


Figure A15. Figure A14 continuation.

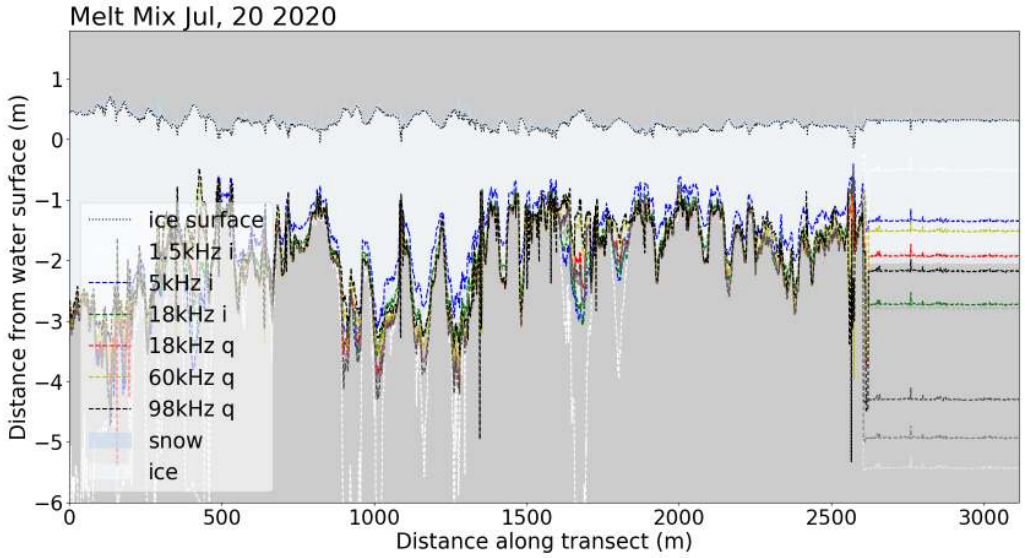


Figure A16. Figure A14 continuation.

Acknowledgements. This work was carried out and the data used in this paper were produced as part of the international Multidisciplinary drifting Observatory for the Study of the Arctic Climate (MOSAiC) with the tag MOSAiC20192020. We thank all persons involved in the expedition of the RV *Polarstern* (Alfred-Wegener-Institut Helmholtz-Zentrum für Polar- und Meeresforschung, 2017) during MOSAiC in 2019–2020 (AWI_PS122_00) as listed in Nixdorf et al. (2021).

The GEM-2 data analysis code was written by Stefan Hendricks (AWI).

We are deeply grateful to all bear guards from all the science and logistic teams. We thank the logistic team, captain and his crew, and cruise leaders during the winter legs of MOSAiC, Christian Haas and Torsten Kanzow for their inexhaustible patience, advice and support. We are also exceptionally grateful to Egor Shimanchuk who was an essential helper for the winter ridge drilling.

This study has been partly funded by the international Multidisciplinary drifting Observatory for the Study of the Arctic Climate (MOSAiC) project with the tag MOSAiC20192020 and the Project_ID: AWI_PS122_00. PI was funded by Research Council of Norway grants #287871 (SIDRiFT) and #343069 (DynAMIC). ES was funded through Research Council of Norway grant #280292 (HAVOC) and #328957 (INTERAAC). CK, RR and AJ were funded by the AWI through the project AWI_ICE. DD was funded through EU-ARICE project DEARice and Research Council of Norway grant #280292 (HAVOC). IR was supported by NSF grant OPP-1724540. The processing of ALS data and the work of AJ were supported by the German Ministry of Research, Technology and Space (BMFTR) grant 03F0866A (IceSense). AJ acknowledges support also by the Research Council of Finland grants 341550 (CROS-Arctic) and 369647 (SNOWBALL). RR was supported by ESA CCI Sea Ice (CCN-2 to Contract 4000126449/19/I-NB -Sea_Ice_cci), the Fram Centre project "Sustainable Development of the Arctic Ocean" (SUDARCO) (project_ID: 2551323), and the Research Council of Norway project TARDIS (grant #325241).

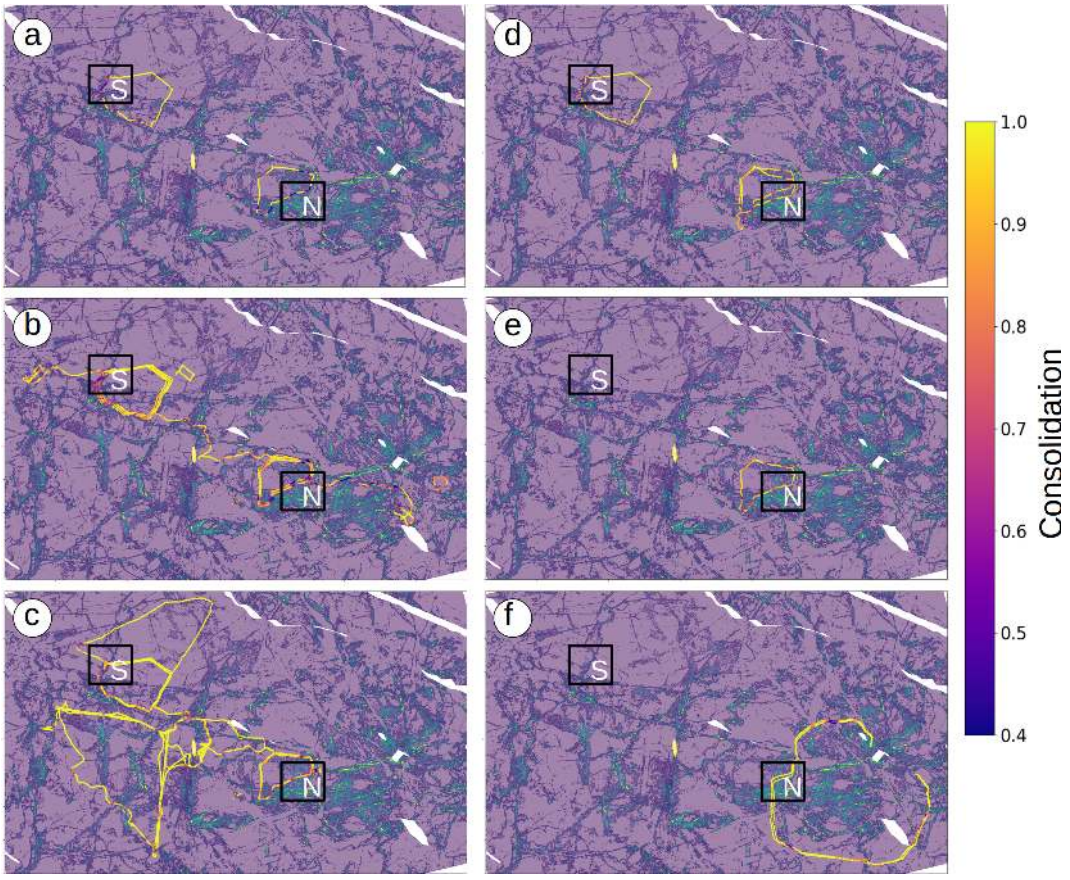


Figure A17. Maps of ridge consolidation for sled transects in the CO from a) December, b) January, c) February, d) March, e) April and f) June. The ridges in Sloop (S) and Nloop (N) that were used for time series are marked by a black square. The ALS freeboard map in the background is from 21 January 2020, with identical colormap, extent and orientation as in Figure 3.

References

Alfred-Wegener-Institut Helmholtz-Zentrum für Polar- und Meeresforschung: Polar research and supply vessel Polarstern operated by the Alfred-Wegener-Institute, Journal of large-scale research facilities JLSRF, 3, A119, https://doi.org/10.17815/jlsrf-3-163, 2017.

Amundrud, T. L., Melling, H., Ingram, R. G., and Allen, S. E.: The effect of structural porosity on the ablation of sea ice ridges, Journal of Geophysical Research: Oceans, 111, C06 004, https://doi.org/10.1029/2005JC002895, 2006.

Anhaus, P., Katlein, C., Arndt, S., Krampe, D., Lange, B. A., Matero, I., Salganik, E., and Nicolaus, M.: Under-ice environment observations from a remotely operated vehicle during the MOSAiC expedition, Scientific Data, 12, 944, https://doi.org/10.1038/s41597-025-05223-1, 2025.

Brenner, S., Rainville, L., Thomson, J., Cole, S., and Lee, C.: Comparing Observations and Parameterizations of Ice-Ocean Drag Through an Annual Cycle Across the Beaufort Sea, Journal of Geophysical Research: Oceans, 126, e2020JC016 977, https://doi.org/10.1029/2020JC016977, 2021.

Castellani, G., Granskog, M. A., Elias Chereque, A., Chan, A. C. Y., Perez, I., Flores, H., Katlein, C., and Peeken, I.: Arctic sea-ice ridges: a major contributor to algal habitable space in spring, Frontiers in Marine Science, 12, 1653 882, https://doi.org/10.3389/fmars.2025.1653882, 2025.

Coppolaro, V.: Sea ice underside three-dimensional topography and draft measurements with an upward-looking multibeam sonar mounted on a remotely operated vehicle, Master's thesis, University of Florence, https://doi.org/10.13140/RG.2.2.34572.95362, 2018.

Cox, C., Gallagher, M., Shupe, M., Persson, O., Grachev, A., Solomon, A., Ayers, T., Costa, D., Hutchings, J., Leach, J., Morris, S., Osborn, J., Pezoa, S., and Uttal, T.: Atmospheric Surface Flux Station 30 measurements (Level 3 Final), Multidisciplinary Drifting Observatory for the Study of Arctic Climate (MOSAiC), central Arctic, October 2019 - September 2020., https://doi.org/10.18739/A2FF3M18K, 2023a.

Cox, C. J., Gallagher, M. R., Shupe, M. D., Persson, P. O. G., Solomon, A., Fairall, C. W., Ayers, T., Blomquist, B., Brooks, I. M., Costa, D., Grachev, A., Gottas, D., Hutchings, J. K., Kutchenreiter, M., Leach, J., Morris, S. M., Morris, V., Osborn, J., Pezoa, S., Preußer, A., Riihimaki, L. D., and Uttal, T.: Continuous observations of the surface energy budget and meteorology over the Arctic sea ice during MOSAiC, Scientific Data, 10, 519, https://doi.org/10.1038/s41597-023-02415-5, 2023b.

Divine, D. V., Gerland, S., and Granskog, M. A.: Sea-ice ridges are a major component of Arctic sea-ice export through the Fram Strait, EGUsphere, 2025, 1–29, https://doi.org/10.5194/egusphere-2025-5511, 2025.

Eicken, H., Tucker, W. B., and Perovich, D. K.: Indirect measurements of the mass balance of summer Arctic sea ice with an electromagnetic induction technique, Annals of Glaciology, 33, 194–200, https://doi.org/10.3189/172756401781818356, 2001.

Ekeberg, O.-C., Høyland, K., and Hansen, E.: Ice ridge keel geometry and shape derived from one year of upward looking sonar data in the Fram Strait, Cold Regions Science and Technology, 109, 78–86, https://doi.org/10.1016/j.coldregions.2014.10.003, 2015.

Ervik, Å., Nord, T. S., Høyland, K. V., Samardzija, I., and Li, H.: Ice-ridge interactions with the Norströmsgrund lighthouse: Global forces and interaction modes, Cold Regions Science and Technology, 158, 195–220, https://doi.org/10.1016/j.coldregions.2018.08.020, 2019.

Gradinger, R., Bluhm, B., and Iken, K.: Arctic sea-ice ridges—Safe heavens for sea-ice fauna during periods of extreme ice melt?, Deep Sea Research Part II, 57, 86–95, https://doi.org/10.1016/j.dsr2.2009.08.008, 2010.

Granskog, M. A., Høyland, K. V., De La Torre, P. R., Divine, D. V., Katlein, C., Itkin, P., Raphael, I., and Olsen, L. M.: Temperature and heating induced temperature difference measurements from the sea ice mass balance buoy SIMBA 2020T60, https://doi.org/10.1594/PANGAEA.924269, 2020.

Granskog, M. A., Berge, J., Cottier, F., Divine, D. V., Katlein, C., Itkin, P., Olsen, L. M., Vogedes, D., and De La Torre, P. R.: Temperature and heating induced temperature difference measurements from the sea ice mass balance buoy SIMBA 2020T61, https://doi.org/10.1594/PANGAEA.926580, 2021.

Guo, W., Itkin, P., Singha, S., Doulgeris, A. P., Johansson, M., and Spreen, G.: Sea ice classification of TerraSAR-X ScanSAR images for the MOSAiC expedition incorporating per-class incidence angle dependency of image texture, The Cryosphere, 17, 1279–1297, https://doi.org/10.5194/tc-17-1279-2023, 2023.

Guzenko, R., May, R., Gavrilov, Y., Kharitonov, V., and Khotchenkov, S.: Evolution of morphometry and internal structure of first-year ridge during many months of observations at the drifting station North Pole-41, in: Proceedings of The Thirty-fourth (2024) International Offshore and Polar Engineering Conference, pp. 2023–2029, Rhodes, Greece,, 2024.

Guzenko, R. B., Gavrilov, Y. G., Kharitonov, V. V., Khotchenkov, S. V., and May, R. I.: Formation and Consolidation of a First-year Ridge Based on Nine Months of Observations at the Drifting Station "North Pole-41", International Journal of Offshore and Polar Engineering, 35, 130–137, https://doi.org/10.17736/ijope.2025.jc943, 2025.

Guzenko, R. B., Mironov, Y. U., May, R. I., Porubaev, V. S., Gavrilov, Y. G., Khotchenkov, S. V., Kornishin, K. A., and Efimov, Y. O.: Morphometry and internal structure of large ice ridges and stamukhas in the Kara, Laptev and East Siberian seas, Journal of Ocean Engineering and Science, 11, 1630–1652, https://doi.org/https://doi.org/10.1016/j.joes.2026.03.004, 2026.

Haas, C. and Rabe, B.: The Expedition PS122/2 of the Research Vessel POLARSTERN to the Arctic Ocean in 2019/2020, https://hdl.handle.net/10013/epic.a9b9fb18-60bc-4550-ba71-10399aa90524, 2023.

Haas, C., Gerland, S., Eicken, H., and Miller, H.: Comparison of sea-ice thickness measurements under summer and winter conditions in the Arctic using a small electromagnetic induction device, GEOPHYSICS, 62, 749–757, https://doi.org/10.1190/1.1444184, 1997.

Hansen, E., Gerland, S., Granskog, M. A., Pavlova, O., Renner, A. H. H., Haapala, J., Løyning, T. B., and Tschudi, M.: Thinning of Arctic sea ice observed in Fram Strait: 1990–2011, Journal of Geophysical Research: Oceans, 118, 5202–5221, https://doi.org/10.1002/jgrc.20393, 2013.

Hansen, E., Ekeberg, O.-C., Gerland, S., Pavlova, O., Spreen, G., and Tschudi, M.: Variability in categories of Arctic sea ice in Fram Strait, Journal of Geophysical Research: Oceans, 119, 7175–7189, https://doi.org/10.1002/2014JC010048, 2014.

Hendricks, S.: Validierung von altimetrischen Meereisdickenmessungen mit einem helikopter-basierten elektromagnetischen Induktionsverfahren, Ph.D. thesis, University Bremen, http://hdl.handle.net/10013/epic.33191.d001, 2009.

Hendricks, S., Itkin, P., Ricker, R., Webster, M., von Albedyll, L., Rohde, J., Raphael, I., Jaggi, M., and Arndt, S.: GEM-2 quicklook total thickness measurements from the 2019-2020 MOSAiC expedition, https://doi.org/10.1594/PANGAEA.943666, 2022.

Hoppmann, M., Richter, M. E., Smith, I. J., Jendersie, S., Langhorne, P. J., Thomas, D. N., and Dieckmann, G. S.: Platelet ice, the Southern Ocean's hidden ice: a review, Annals of Glaciology, 61, 341–368, https://doi.org/10.1017/aog.2020.54, 2020.

Hunkeler, P. A., Hendricks, S., Hoppmann, M., Paul, S., and Gerdes, R.: Towards an estimation of sub-sea-ice platelet-layer volume with multi-frequency electromagnetic induction sounding, Annals of Glaciology, 56, 137–146, https://doi.org/10.3189/2015AoG69A705, 2015.

Hunkeler, P. A., Hendricks, S., Hoppmann, M., Farquharson, C. G., Kalscheuer, T., Grab, M., Kaufmann, M. S., Rabenstein, L., and Gerdes, R.: Improved 1D inversions for sea ice thickness and conductivity from electromagnetic induction data: Inclusion of nonlinearities caused by passive bucking, Geophysics, 81, WA45–WA58, https://doi.org/10.1190/geo2015-0130.1, 2016.

Hutter, N., Hendricks, S., Jutila, A., Birnbaum, G., von Albedyll, L., Ricker, R., and Haas, C.: Merged grids of sea-ice or snow freeboard from helicopter-borne laser scanner during the MOSAiC expedition, version 1, https://doi.org/10.1594/PANGAEA.950896, 2023a.

Hutter, N., Hendricks, S., Jutila, A., Ricker, R., von Albedyll, L., Birnbaum, G., and Haas, C.: Digital elevation models of the sea-ice surface from airborne laser scanning during MOSAiC, Scientific Data, 10, https://doi.org/10.1038/s41597-023-02565-6, 2023b.

Høyland, K. V.: Consolidation of first-year sea ice ridges, Journal of Geophysical Research: Oceans, 107, 15–1–15–16, https://doi.org/10.1029/2000JC000526, 2002.

Itkin, P.: Novel methods to study sea ice deformation, linear kinematic features and coherent dynamic clusters from imaging remote sensing data, The Cryosphere, 19, 1135–1151, https://doi.org/10.5194/tc-19-1135-2025, 2025.

Itkin, P. and Liston, G. E.: Combining observational data and numerical models to obtain a seamless high temporal resolution seasonal cycle of snow and ice mass balance at the MOSAiC Central Observatory, EGUsphere, 2024, 1–36, https://doi.org/10.5194/egusphere-2024-3402, 2024.

Itkin, P. and Liston, G. E.: Combining observational data and numerical models to obtain a seamless high-temporal-resolution seasonal cycle of snow and ice mass balance at the MOSAiC Central Observatory, The Cryosphere, 19, 5111–5133, https://doi.org/10.5194/tc-19-5111-2025, 2025.

Itkin, P., Spreen, G., Cheng, B., Doble, M., Girard-Ardhuin, F., Haapala, J., Hughes, N., Kaleschke, L., Nicolaus, M., and Wilkinson, J.: Thin ice and storms: Sea ice deformation from buoy arrays deployed during N-ICE2015, Journal of Geophysical Research: Oceans, 122, 4661–4674, https://doi.org/10.1002/2016JC012403, 2017.

Itkin, P., Webster, M., Hendricks, S., Oggier, M., Jaggi, M., Ricker, R., Arndt, S., Divine, D. V., von Albedyll, L., Raphael, I., Rohde, J., and Liston, G. E.: Magnaprobe snow and melt pond depth measurements from the 2019-2020 MOSAiC expedition, https://doi.org/10.1594/PANGAEA.937781, 2021.

Itkin, P., Hendricks, S., Webster, M., von Albedyll, L., Arndt, S., Divine, D., Jaggi, M., Oggier, M., Raphael, I., Ricker, R., Rohde, J., Schneebeli, M., and Liston, G. E.: Sea ice and snow characteristics from year-long transects at the MOSAiC Central Observatory, Elementa: Science of the Anthropocene, 11, 00 048, https://doi.org/10.1525/elementa.2022.00048, 2023.

Jackson, K., Wilkinson, J., Maksym, T., Meldrum, D., Beckers, J., Haas, C., and Mackenzie, D.: A Novel and Low-Cost Sea Ice Mass Balance Buoy, Journal of Atmospheric and Oceanic Technology, 30, 2676–2688, https://doi.org/10.1175/JTECH-D-13-00058.1, 2013.

Jutila, A., Hendricks, S., Ricker, R., von Albedyll, L., Krumpen, T., and Haas, C.: Retrieval and parameterisation of sea-ice bulk density from airborne multi-sensor measurements, The Cryosphere, 16, 259–275, https://doi.org/10.5194/tc-16-259-2022, 2022.

Kanzow, T. and Damm, E.: The Expedition PS122/3 of the Research Vessel POLARSTERN to the Arctic Ocean in 2020, https://hdl.handle.net/10013/epic.58b0f57c-f075-4b24-8b76-07d3f0eec87d, 2023.

Katlein, C., Schiller, M., Belter, H. J., Coppolaro, V., Wenslandt, D., and Nicolaus, M.: A New Remotely Operated Sensor Platform for Interdisciplinary Observations under Sea Ice, Frontiers in Marine Science, 4, https://doi.org/10.3389/fmars.2017.00281, 2017.

Katlein, C., Mohrholz, V., Sheikin, I., Itkin, P., Divine, D. V., Stroeve, J., Jutila, A., Krampe, D., Shimanchuk, E., Raphael, I., Rabe, B., Kuznetsov, I., Mallet, M., Liu, H., Hoppmann, M., Fang, Y.-C., Dumitrascu, A., Arndt, S., Anhaus, P., Nicolaus, M., Matero, I., Oggier, M., Eicken, H., and Haas, C.: Platelet ice under Arctic pack ice in winter, Geophysical Research Letters, 47, e2020GL088 898, https://doi.org/10.1029/2020GL088898, 2020.

Katlein, C., Anhaus, P., Arndt, S., Krampe, D., Lange, B. A., Matero, I., Regnery, J., Rohde, J., Schiller, M., and Nicolaus, M.: Sea-ice draft during the MOSAiC expedition 2019/20, https://doi.org/10.1594/PANGAEA.945846, 2022.

Kharitonov, V. V.: Peculiarities of Fractional Composition of the Pechora Sea First-Year Ridges, in: Proceedings of the International Conference on Port and Ocean Engineering under Arctic Conditions, POAC'05, pp. 907–916, Potsdam New York, United States, 2005.

Kortum, K., Singha, S., Spreen, G., Hutter, N., Jutila, A., and Haas, C.: SAR deep learning sea ice retrieval trained with airborne laser scanner measurements from the MOSAiC expedition, The Cryosphere, 18, 2207–2222, https://doi.org/10.5194/tc-18-2207-2024, 2024.

Krumpen, T., Haapala, J., Krocker, R., and Bartsch, A.: Ice radar raw data (sigma S6 ice radar) of RV POLARSTERN during cruise PS122/1, https://doi.org/10.1594/PANGAEA.929434, 2021a.

Krumpen, T., Hutchings, J. K., Krocker, R., and Bartsch, A.: Ice radar raw data (sigma S6 ice radar) of RV POLARSTERN during cruise PS122/3, https://doi.org/10.1594/PANGAEA.929438, 2021b.

Krumpen, T., Itkin, P., Krocker, R., and Bartsch, A.: Ice radar raw data (sigma S6 ice radar) of RV POLARSTERN during cruise PS122/2, https://doi.org/10.1594/PANGAEA.929435, 2021c.

Krumpen, T., von Albedyll, L., Bünger, H. J., Castellani, G., Hartmann, J., Helm, V., Hendricks, S., Hutter, N., Landy, J. C., Lisovski, S., Lüpkes, C., Rohde, J., Suhrhoff, M., and Haas, C.: Smoother sea ice with fewer pressure ridges in a more dynamic Arctic, Nature Climate Change, https://doi.org/10.1038/s41558-024-02199-5, 2025.

Landy, J. C., Petty, A. A., Tsamados, M., and Stroeve, J. C.: Sea Ice Roughness Overlooked as a Key Source of Uncertainty in CryoSat-2 Ice Freeboard Retrievals, Journal of Geophysical Research: Oceans, 125, e2019JC015 820, https://doi.org/10.1029/2019jc015820, 2020.

Lange, B. A., Salganik, E., Macfarlane, A. R., Schneebeli, M., Høyland, K. V., Gardner, J., Müller, O., and Granskog, M. A.: Ridge ice oxygen and hydrogen isotope data MOSAiC Leg 4 (PS122/4), https://doi.org/10.1594/PANGAEA.943746, 2022.

Lange, B. A., Salganik, E., Macfarlane, A., Schneebeli, M., Høyland, K., Gardner, J., Müller, O., Divine, D. V., Kohlbach, D., Katlein, C., and Granskog, M. A.: Snowmelt contribution to Arctic first-year ice ridge mass balance and rapid consolidation during summer melt, Elementa: Science of the Anthropocene, 11, 00 037, https://doi.org/10.1525/elementa.2022.00037, 2023.

Lange, K. A., Bradley, A. C., Duncan, K., and Farrell, S. L.: Grounded ridge detection and characterization along the Alaska Arctic coastline using ICESat-2 surface height retrievals, The Cryosphere, 19, 2045–2065, https://doi.org/10.5194/tc-19-2045-2025, 2025.

Leppäranta, M. and Hakala, R.: The structure and strength of first-year ice ridges in the Baltic Sea, Cold Regions Science and Technology, 20, 295–311, https://doi.org/10.1016/0165-232x(92)90036-t, 1992.

Macfarlane, A. R., Tavri, A., Polashenski, C., Krampe, D., Seawell, D. C., Wagner, D. N., Shimanchuck, E., Hannula, H.-R., Raphael, I., Mateo, I., Regnery, J., Smith, M., Oggier, M., Nicolaus, M., Jaggi, M., Lehning, M., Kolabutin, N., Pirazzini, R., Dadic, R., Hammerle, S., Arndt, S., and Schneebeli, M.: Snowpit raw data during the MOSAiC expedition, https://doi.org/10.1594/PANGAEA.935934, 2021.

Macfarlane, A. R., Löwe, H., Gimenes, L., Wagner, D. N., Dadic, R., Ottersberg, R., Hämmerle, S., and Schneebeli, M.: Temporospatial variability of snow's thermal conductivity on Arctic sea ice, The Cryosphere, 17, 5417–5434, https://doi.org/10.5194/tc-17-5417-2023, 2023.

Marchenko, A.: Modeling of Thermodynamic Consolidation of Sea Ice Ridges Drifting in the Water with Changing Temperature, Journal of Marine Science and Engineering, 10, https://doi.org/10.3390/jmse10121858, 2022.

Mchedlishvili, A., Lüpkes, C., Petty, A., Tsamados, M., and Spreen, G.: New estimates of pan-Arctic sea ice–atmosphere neutral drag coefficients from ICESat-2 elevation data, The Cryosphere, 17, 4103–4131, https://doi.org/10.5194/tc-17-4103-2023, 2023.

Melling, H. and Riedel, D. A.: Development of seasonal pack ice in the Beaufort Sea during the winter of 1991–1992: A view from below, Journal of Geophysical Research: Oceans, 101, 11 975–11 991, https://doi.org/10.1029/96JC00284, 1996.

Merkouriadi, I., Liston, G. E., Graham, R. M., and Granskog, M. A.: Quantifying the Potential for Snow-Ice Formation in the Arctic Ocean, Geophysical Research Letters, 47, e2019GL085 020, https://doi.org/10.1029/2019GL085020, 2020.

Müller, O., Gardner, J., Olsen, L. M., Salganik, E., Assmy, P., Gradinger, R., Bratbak, G., Hoppe, C. J. M., Lange, B. A., Muilwijk, M., Divine, D. V., Aberle, N., Krause, J., Reigstad, M., Leu, E., Tsagaraki, T. M., Larsen, A., Høyland, K. V., Balmonte, J. P., Boulton, W., Dahle, H., Eggers, L., Fong, A. A., Guillou, G., Lebreton, B., Metfies, K., Mock, T., Petelenz, E., Tatarek, A., Torres-Valdes, S., Torstensson, A., Wiktor, J., and Granskog, M. A.: Arctic sea-ice ridges are biomass hotspots harboring diverse microbial communities, Communications Earth & Environment, 7, 385, https://doi.org/10.1038/s43247-026-03364-8, 2026.

Neudert, M., Arndt, S., Hendricks, S., Hoppmann, M., Schulze, M., and Haas, C.: Improved sub-ice platelet layer mapping with multi-frequency EM induction sounding, Journal of Applied Geophysics, 230, 105 540, https://doi.org/10.1016/j.jappgeo.2024.105540, 2024.

Nicolaus, M., Perovich, D. K., Spreen, G., Granskog, M. A., von Albedyll, L., Angelopoulos, M., Anhaus, P., Arndt, S., Belter, H. J., Bessonov, V., Birnbaum, G., Brauchle, J., Calmer, R., Cardellach, E., Cheng, B., Clemens-Sewall, D., Dadic, R., Damm, E., de Boer, G., Demir, O., Dethloff, K., Divine, D. V., Fong, A. A., Fons, S., Frey, M. M., Fuchs, N., Gabarró, C., Gerland, S., Goessling, H. F., Gradinger, R., Haapala, J., Haas, C., Hamilton, J., Hannula, H.-R., Hendricks, S., Herber, A., Heuzé, C., Hoppmann, M., Høyland, K. V., Huntemann, M., Hutchings, J. K., Hwang, B., Itkin, P., Jacobi, H.-W., Jaggi, M., Jutila, A., Kaleschke, L., Katlein, C., Kolabutin, N., Krampe, D., Kristensen, S. S., Krumpen, T., Kurtz, N., Lampert, A., Lange, B. A., Lei, R., Light, B., Linhardt, F., Liston, G. E., Loose, B., Macfarlane, A. R., Mahmud, M., Matero, I. O., Maus, S., Morgenstern, A., Naderpour, R., Nandan, V., Niubom, A., Oggier, M., Oppelt, N., Pätzold, F., Perron, C., Petrovsky, T., Pirazzini, R., Polashenski, C., Rabe, B., Raphael, I. A., Regnery, J., Rex, M., Ricker, R., Riemann-Campe,

K., Rinke, A., Rohde, J., Salganik, E., Scharien, R. K., Schiller, M., Schneebeli, M., Semmling, M., Shimanchuk, E., Shupe, M. D., Smith, M. M., Smolyanitsky, V., Sokolov, V., Stanton, T., Stroeve, J., Thielke, L., Timofeeva, A., Tonboe, R. T., Tavri, A., Tsamados, M., Wagner, D. N., Watkins, D., Webster, M., and Wendisch, M.: Overview of the MOSAiC expedition: snow and sea ice, Elementa: Science of the Anthropocene, 10, 000 046, https://doi.org/10.1525/elementa.2021.000046, 2022.

Nixdorf, U., Dethloff, K., Rex, M., Shupe, M., Sommerfeld, A., Perovich, D. K., Nicolaus, M., Heuzé, C., Rabe, B., Loose, B., Damm, E., Gradinger, R., Fong, A., Maslowski, W., Rinke, A., Kwok, R., Spreen, G., Wendisch, M., Herber, A., Hirsekorn, M., Mohaupt, V., Frickenhaus, S., Immerz, A., Weiss-Tuider, K., König, B., Mengedoht, D., Regnery, J., Gerchow, P., Ransby, D., Krumpen, T., Morgenstern, A., Haas, C., Kanzow, T., Rack, F. R., Saitzev, V., Sokolov, V., Makarov, A., Schwarze, S., Wunderlich, T., Wurr, K., and Boetius, A.: MOSAiC Extended Acknowledgement, https://doi.org/10.5281/zenodo.5541624, 2021.

Oikkonen, A., Haapala, J., Lensu, M., Karvonen, J., and Itkin, P.: Small-scale sea ice deformation during N-ICE2015: From compact pack ice to marginal ice zone, Journal of Geophysical Research: Oceans, 122, 5105–5120, https://doi.org/10.1002/2016jc012387, 2017.

Ólason, E., Boutin, G., Williams, T., Korosov, A., Regan, H., Rheinlænder, J., Rampal, P., Flocco, D., Samaké, A., Davy, R., Spain, T., and Chua, S.: The next generation sea-ice model neXtSIM, version 2, Geoscientific Model Development, 19, 6467–6496, https://doi.org/10.5194/gmd-19-6467-2026, 2026.

Perovich, D. K., Grenfell, T. C., Richter-Menge, J. A., Light, B., Tucker III, W. B., and Eicken, H.: Thin and thinner: sea ice mass balance measurements during SHEBA, Journal of Geophysical Research: Oceans, 108, 8050, https://doi.org/10.1029/2001JC001079, 2003.

Petty, A., Cabaj, A., and Landy, J. C.: Initial assessment of all-season Arctic sea ice thickness from ICESat-2, Journal of Glaciology, 72, e4, https://doi.org/10.1017/jog.2025.10119, 2026.

Petty, A. A., Tsamados, M. C., and Kurtz, N. T.: Atmospheric form drag coefficients over Arctic sea ice using remotely sensed ice topography data, spring 2009–2015, J. Geophys. Res.: Earth Surface, 122, 1472–1490, https://doi.org/10.1002/2017JF004209, 2017.

Pfaffling, A., Haas, C., and Reid, J. E.: Direct helicopter EM — Sea-ice thickness inversion assessed with synthetic and field data, GEOPHYSICS, 72, F127–F137, https://doi.org/10.1190/1.2732551, 2007.

Provost, C., Sennéchael, N., Miguet, J., Itkin, P., Rösel, A., Koenig, Z., Villacieros-Robineau, N., and Granskog, M. A.: Observations of flooding and snow-ice formation in a thinner Arctic sea-ice regime during the N-ICE2015 campaign: influence of basal ice melt and storms, Journal of Geophysical Research: Oceans, 122, 7115–7134, https://doi.org/10.1002/2016JC012011, 2017.

Rampal, P., Weiss, J., and Marsan, D.: Positive trend in the mean speed and deformation rate of Arctic sea ice, 1979–2007, Journal of Geophysical Research: Oceans, 114, C05 013, https://doi.org/10.1029/2008JC005066, 2009.

Reid, J. E. and Vrbancich, J.: A comparison of the inductive-limit footprints of airborne electromagnetic configurations, Geophysics, 69, 1229–1239, https://doi.org/10.1190/1.1801939, 2004.

Reid, J. E., Worby, A. P., Vrbancich, J., and Munro, A. I. S.: Shipborne electromagnetic measurements of Antarctic sea-ice thickness, GEOPHYSICS, 68, 1537–1546, https://doi.org/10.1190/1.1620627, 2003.

Renner, A. H. H., Gerland, S., Haas, C., Spreen, G., Beckers, J. F., Hansen, E., Nicolaus, M., and Goodwin, H.: Evidence of Arctic sea ice thinning from direct observations, Geophysical Research Letters, 41, 5029–5036, https://doi.org/10.1002/2014gl060369, 2014.

Rex, M. and Nicolaus, M.: The Expedition PS122/1 of the Research Vessel POLARSTERN to the Arctic Ocean in 2019, https://hdl.handle.net/10013/epic.8346761b-a10c-47c2-84cf-da26c6c3c5e2, 2023.

Rheinlænder, J. W., Regan, H., Rampal, P., Boutin, G., Ólason, E., and Davy, R.: Breaking the Ice: Exploring the Changing Dynamics of Winter Breakup Events in the Beaufort Sea, Journal of Geophysical Research: Oceans, 129, e2023JC020 395, https://doi.org/10.1029/2023JC020395, 2024.

Richter-Menge, J. A. and Cox, G. F. N.: Structure, salinity and density of multi-year sea ice pressure ridges, in: Proc. Fourth International Offshore Mechanics and Arctic Engineering Symposium, edited by Chung, J. S., pp. 194–198, New York, NY, 1985.

Ricker, R., Fons, S., Jutila, A., Hutter, N., Duncan, K., Farrell, S. L., Kurtz, N. T., and Fredensborg Hansen, R. M.: Linking scales of sea ice surface topography: evaluation of ICESat-2 measurements with coincident helicopter laser scanning during MOSAiC, The Cryosphere, 17, 1411–1429, https://doi.org/10.5194/tc-17-1411-2023, 2023.

Rösel, A., Itkin, P., King, J., Divine, D., Wang, C., Granskog, M. A., Krumpen, T., and Gerland, S.: Thin sea ice, thick snow, and widespread negative freeboard observed during N-ICE2015 north of Svalbard, Journal of Geophysical Research: Oceans, 123, 1156–1176, https://doi.org/10.1002/2017JC012865, 2018.

Salganik, E., Høyland, K. V., and Shestov, A.: Medium-scale experiment in consolidation of an artificial sea ice ridge in Van Mijenfjorden, Svalbard, Cold Regions Science and Technology, 181, 103 194, https://doi.org/10.1016/j.coldregions.2020.103194, 2021.

Salganik, E., Lange, B. A., Divine, D. V., Itkin, P., Katlein, C., Høyland, K. V., and Granskog, M. A.: Drill-hole ridge ice and snow thickness and draft measurements during MOSAiC 2019/20, https://doi.org/10.1594/PANGAEA.950192, 2022.

Salganik, E., Hoppmann, M., Scholz, D., Arndt, S., Demir, O., Divine, D. V., Haapala, J., Hendricks, S., Itkin, P., Katlein, C., Kolabutin, N., Lei, R., Matero, I., Nicolaus, M., Raphael, I., Regnery, J., Oggier, M., Sheikin, I., Shimanchuk, E., and Spreen, G.: Temperature and heating induced temperature difference measurements from Digital Thermistor Chains (DTCs) during MOSAiC 2019/2020, https://doi.org/10.1594/PANGAEA.964023, 2023.

Salganik, E., Itkin, P., Divine, D. V., Katlein, C., Høyland, K. V., and Granskog, M. A.: Drill-hole ridge ice and snow thickness and draft measurements of "Fort Ridge" during MOSAiC 2019/20, https://doi.org/10.1594/PANGAEA.960347, 2023a.

Salganik, E., Itkin, P., Divine, D. V., Olsen, L. M., Shimanchuk, E., and Granskog, M. A.: Ice salinity measurements of Fort Ridge during MOSAiC 2019/20, https://doi.org/10.1594/PANGAEA.962542, 2023b.

Salganik, E., Lange, B. A., Høyland, K. V., Gardner, J., Müller, O., Tavri, A., Mahmud, M., and Granskog, M. A.: Ridge ice density data MOSAiC Leg 4 (PS122/4), https://doi.org/10.1594/PANGAEA.953865, 2023c.

Salganik, E., Lange, B. A., Itkin, P., Divine, D., Katlein, C., Nicolaus, M., Hoppmann, M., Neckel, N., Ricker, R., Høyland, K. V., and Granskog, M. A.: Different mechanisms of Arctic first-year sea-ice ridge consolidation observed during the MOSAiC expedition, Elementa: Science of the Anthropocene, 11, 00 008, https://doi.org/10.1525/elementa.2023.00008, 2023d.

Salganik, E., Lange, B. A., Katlein, C., Matero, I., Anhaus, P., Muilwijk, M., Høyland, K. V., and Granskog, M. A.: Observations of preferential summer melt of Arctic sea-ice ridge keels from repeated multibeam sonar surveys, The Cryosphere, 17, 4873–4887, https://doi.org/10.5194/tc-17-4873-2023, 2023e.

Salganik, E., Crabeck, O., Fuchs, N., Hutter, N., Anhaus, P., and Landy, J. C.: Impacts of air fraction increase on Arctic sea ice density, freeboard, and thickness estimation during the melt season, The Cryosphere, 19, 1259–1278, https://doi.org/10.5194/tc-19-1259-2025, 2025.

Schulz, K., Mohrholz, V., Fer, I., Janout, M. A., Hoppmann, M., Schaffer, J., Koenig, Z., Rabe, B., Heuzé, C., Regnery, J., Allerholt, J., Fang, Y.-C., He, H., Kanzow, T., Karam, S., Kuznetsov, I., Kong, B., Liu, H., Muilwijk, M., Schuffenhauer, I., Sukhikh, N., Sundfjord, A., and Tippenhauer, S.: Turbulent microstructure profile (MSS) measurements from the MOSAiC drift, Arctic Ocean, https://doi.org/10.1594/PANGAEA.939816, dataset, 2022.

Schulz, K., Koenig, Z., Muilwijk, M., Bauch, D., Hoppe, C. J. M., Droste, E. S., Hoppmann, M., Chamberlain, E. J., Laukert, G., Stanton, T., Quintanilla-Zurita, A., Fer, I., Heuzé, C., Karam, S., Mieruch-Schnülle, S., Baumann, T. M., Vredenborg, M., Tippenhauer, S.,

and Granskog, M. A.: The Eurasian Arctic Ocean along the MOSAiC drift in 2019–2020: An interdisciplinary perspective on physical properties and processes, Elementa: Science of the Anthropocene, 12, 00 114, https://doi.org/10.1525/elementa.2023.00114, 2024.

Shafrova, S. and Høyland, K. V.: Morphology and 2D spatial strength distribution in two Arctic first-year sea ice ridges, Cold Regions Science and Technology, 51, 38–55, https://doi.org/10.1016/j.coldregions.2007.05.011, 2008.

Shestov, A., Høyland, K. V., and Ekeberg, O.-C.: Morphology and Physical Properties of Old Sea Ice in the Fram Strait 2006-2011, in: Proc. 21st IAHR International Symposium on Ice, p. Paper no. 83, https://www.iahr.org/library/infor?pid=27090, 2012.

Shestov, A., Høyland, K., and Åse Ervik: Decay phase thermodynamics of ice ridges in the Arctic Ocean, Cold Regions Science and Technology, 152, 23–34, https://doi.org/10.1016/j.coldregions.2018.04.005, 2018.

Shupe, M. D., Rex, M., Dethloff, K., Damm, E., Fong, A. A., Gradinger, R., Heuzé, C., Loose, B., Makarov, A., Maslowski, W., Nicolaus, M., Perovich, D., Rabe, B., Rinke, A., Sokolov, V., and Sommerfeld, A.: Arctic Report Card 2020: the MOSAiC expedition: a year drifting with the Arctic sea ice, Arctic Report Card, https://doi.org/10.25923/9g3v-xh92, 2020.

Smith, M. M., von Albedyll, L., Raphael, I. A., Lange, B. A., Matero, I., Salganik, E., Webster, M. A., Granskog, M. A., Fong, A., Lei, R., and Light, B.: Quantifying false bottoms and under-ice meltwater layers beneath Arctic summer sea ice with fine-scale observations, Elementa: Science of the Anthropocene, 10, 000 116, https://doi.org/10.1525/elementa.2021.000116, 2022.

Smith, M. M., Fuchs, N., Salganik, E., Perovich, D. K., Raphael, I., Granskog, M. A., Schulz, K., Shupe, M. D., and Webster, M.: Formation and fate of freshwater on an ice floe in the Central Arctic, The Cryosphere, 19, 619–644, https://doi.org/10.5194/tc-19-619-2025, 2025.

Spreen, G., Kwok, R., and Menemenlis, D.: Trends in Arctic sea ice drift and role of wind forcing: 1992–2009, Geophysical Research Letters, 38, https://doi.org/10.1029/2011GL048970, 2011.

Strub-Klein, L. and Sudom, D.: A comprehensive analysis of the morphology of first-year sea ice ridges, Cold Regions Science and Technology, 82, 94–109, https://doi.org/10.1016/j.coldregions.2012.05.014, 2012.

Sturm, M. and Holmgren, J.: An automatic snow depth probe for field validation campaigns, Water Resources Research, 54, 9695–9701, https://doi.org/10.1029/2018WR023559, 2018.

Sumata, H., de Steur, L., Divine, D. V., Granskog, M. A., and Gerland, S.: Regime shift in Arctic Ocean sea ice thickness, Nature, 615, 443–449, https://doi.org/10.1038/s41586-022-05686-x, 2023.

Tsamados, M., Feltham, D. L., Schroeder, D., Flocco, D., Farrell, S. L., Kurtz, N., Laxon, S. W., and Bacon, S.: Impact of Variable Atmospheric and Oceanic Form Drag on Simulations of Arctic Sea Ice, Journal of Physical Oceanography, 44, 1329–1353, https://doi.org/10.1175/JPO-D-13-0215.1, 2014.

von Albedyll, L., Hendricks, S., Grodofzig, R., Krumpen, T., Arndt, S., Belter, H., Cheng, B., Birnbaum, G., Hoppmann, M., Hutchings, J., Itkin, P., Lei, R., Nicolaus, M., Ricker, R., Rohde, J., Suhrhoff, M., Timofeeva, A., Watkins, D., Webster, M., and Haas, C.: Thermodynamic and dynamic contributions to seasonal Arctic sea ice thickness distributions from airborne observations, Elementa: Science of the Anthropocene, 10, 00 074, https://doi.org/10.1525/elementa.2021.00074, 2022.

Webster, M. A., Holland, M., Wright, N. C., Hendricks, S., Hutter, N., Itkin, P., Light, B., Linhardt, F., Perovich, D. K., Raphael, I. A., Smith, M. M., von Albedyll, L., and Zhang, J.: Spatiotemporal evolution of melt ponds in the Arctic: MOSAiC observations and model result, Elementa, 10, 000 072, https://doi.org/10.1525/elementa.2021.000072, 2022.